Despeckling SAR Image Quality Evaluation by Homogeneity and Heterogeneity Scene Patches

Chuang Sun, Fengcheng Guo, Zhaoling Hu, Lianpeng Zhang, Wensong Liu, and Tingting Huang

***Abstract*—Synthetic aperture radar (SAR) imaging is hindered by coherent imaging mechanisms, leading to degradation in image quality due to speckle. Current methods can effectively suppress speckles but may lead to varying degrees of edge information loss. The accurate and comprehensive evaluation of speckle suppression is vital for enhancing SAR image interpretation. Therefore, this study proposes a novel method for evaluating despeckling image quality based on adaptively extracting homogeneity and heterogeneity scene patches (IQE_HHSP). The proposed IQE_HHSP effectively extracts homogeneous and heterogeneous patches, and performs speckle suppression and edge-preservation evaluation based on the extracted patch feature, achieving comprehensive evaluation of filtered image. The efficacy of IQE_HHSP is demonstrated through the evaluation on four SAR images using six comparative evaluation indicators. The experimental results indicate that IQE_HHSP provides the accurate quality assessment of SAR filtering models, yielding results consistent with visual observations.**

***Index Terms*—Edge preservation, heterogeneity, homogeneity, patches, speckle, speckle suppression, synthetic aperture radar (SAR).**

I. Introduction

SYNTHETIC aperture radar (SAR) is an active coherent imaging system offering numerous advantages, such as all-time all-weather capability and high penetration, among others. It has emerged as a useful tool supporting economic development, military reconnaissance, urban planning, marine exploration, and ship monitoring. However, SAR images are susceptible to speckles due to coherent imaging systems, which significantly hinder their interpretability, target detection or recognition, and the usefulness in high-quality applications [1], [2], [3], [4], [5]. Consequently, speckle suppression has become a crucial preprocessing task in SAR image applications.

Received 13 June 2024; revised 16 August 2024 and 24 September 2024; accepted 8 October 2024. Date of publication 11 October 2024; date of current version 29 October 2024. This work was supported in part by the National Natural Science Foundation of China under Grant 62101219 and Grant 62201232, in part by the Jiangsu Provincial Natural Science Foundation of China under Grant BK20210921 and Grant BK20201026, in part by the "343" Industrial Development Project for University in Xuzhou under Grant gx2023010, and in part by the Social Welfare Project in Xuzhou City under Grant KC23304. *(Corresponding author: Fengcheng Guo.)*

Chuang Sun, Fengcheng Guo, Zhaoling Hu, Lianpeng Zhang, and Wensong Liu are with the School of Geography, Geomatic and Planning, Jiangsu Normal University, Xuzhou 221116, China (e-mail: 2020231583@jsnu.edu.cn; fchguo@jsnu.edu.cn; huzhaoling@jsnu.edu.cn; zhanglp2000@126.com; liu wensongupc@163.com).

Tingting Huang is with the School of Institute of Surveying, Mapping and Geoinformation, Guilin University of Technology, Guilin 541004, China (e-mail: 1020232083@glut.edu.cn).

Digital Object Identifier 10.1109/JSTARS.2024.3479229

After more than half a century of research, various filtering models have been proposed, broadly categorized into spatial domain-based models [6], [7], [8], [9], [10], transformation domain-based models [11], [12], [13], [14], [15], models employing partial differential equations [16], [17], [18], [19], [20], [21], nonlocal means-based approaches [22], [23], [24], [25], [26], [27], and deep-learning-based methods [28], [29], [30], [31], [32], [33], [32]. While these methods effectively suppress speckles, they often lead to varying degrees of edge information loss. An ideal despeckling filter model should significantly reduce speckle without sacrificing detailed information with the objective of enhancing speckle smoothing while preserving edges. Additionally, objectively evaluating whether a filtering model achieves these objectives poses a key challenge.

Currently, qualitative and quantitative evaluations are the two primary methods for despeckling images [34], [35], [36], [37], [38], [39], [40], [41], [42]. Visual observation serves as an important method for qualitative assessment and is among the most direct and effective strategies. Initially, many works relied on visual inspection of images before and after filtering to assess filtering performance. However, visual observation has inherent limitations, such as the inability to quantitatively describe speckle suppression, edge loss, and susceptibility to subjective human biases. Hence, introducing quantitative evaluation methods is important to obtain more precise assessments of filtered results.

Quantitative evaluation of filtered images primarily focuses on two aspects: speckle suppression and edge preservation. The most commonly used metric for evaluating speckle suppression is the equivalent number of looks (ENL) [34], which estimates the ratio of the square of the sample mean to the sample variance in homogeneous patches, providing a more accurate evaluation of speckle suppression. Another evaluation index for speckle reduction is the speckle suppression index (SSI) [35], which estimates the ratio between the sample coefficients of variation based on homogeneous patches of the image before and after filtering. However, ENL and SSI have limitations. ENL values can increase excessively when the filtered image exhibits oversmoothing, necessitating visual confirmation. Moreover, ENL and SSI reliability depends on the mean-preserving characteristics of filters. Addressing the drawbacks of ENL and SSI, the speckle suppression and mean-preservation index (SMPI) [36] was proposed, providing a better evaluation of stability for poor mean value preservation. However, SMPI is prone to outliers due to the lack of normalization of the mean difference between images before and after filtering, especially in large

backscattered regions. To mitigate this, the mean-preservation speckle suppression index (MPSSI) [37] was developed by normalizing SMPI, enhancing its applicability for comparing different algorithms.

In edge-preservation assessments, the structural similarity (SSIM) [38] is widely regarded as the most effective index. It can effectively assess the similarity maintenance between speckled and filtered images by analyzing brightness, contrast, and structure. The edge-saving index (ESI) [39] reflects the horizontal and vertical edge-preserving abilities of the filtering model. The edge-enhancing index [35] quantifies the edge enhancement effect by comparing edge points and lines before and after filtering. The edge-preservation index [40] characterizes the edge using the gradient sum of the original and smoothed images, while Pratt's figure of merit [41] evaluates edge retention by comparing true feature contours before and after filtering.

Neither the SSI nor the edge information retention index can comprehensively evaluate the advantages and disadvantages of a filtering model from a single aspect. When a filtered image exhibits good speckle reduction but poor edge maintenance, or vice-versa, the above single evaluation models are insufficient. Thus, there is a need for a comprehensive evaluation index that simultaneously considers speckle suppression and edge information retention. Currently, research on comprehensive evaluation indicators is limited, including the M [43], $\alpha\beta$ [44], and structural correlation nonreference evaluation model (SCNREM) [45]. The M [43] metric evaluates both aspects based on the statistical characteristics of the ratio image and the deviation of residual structure content, pioneering evaluation based on the ratio image; however, its experimental results lack stability. The $\alpha\beta$ metric [44] introduces statistical characteristics of the ratio image based on the β metric [45], offering a better comprehensive evaluation of filtering models. However, it is ineffective for models with weak edge retention. SCNREM [46] can comprehensively evaluate speckle suppression and structural information retention using adaptive weights, yet it does not effectively address the issue of determining weights for different evaluation factors. In addition, Di Martino et al. [3] proposed a benchmarking framework for SAR filtering and evaluation, which integrates speckle suppression and evaluation in a wider range of scenarios through simulating SAR datasets.

This study proposes a novel SAR filter quality evaluation indicator based on adaptively extracting homogeneity and heterogeneity scene patches (IQE_HHSP) to address the inadequacy of traditional comprehensive evaluation indices in effectively assigning weights to speckle suppression and edge information retention assessments. IQE_HHSP first establishes an adaptive homogeneous and heterogeneous patch extraction method for complex SAR scenes. Subsequently, it constructs a partition evaluation model considering different patches of the scene. Finally, it determines the weighting method for each index in the partition evaluation model.

II. Basic Methods of Filter Evaluation

The accurate evaluation of the filtering performance of SAR images is crucial for testing the efficacy of speckle suppression models. Most evaluation methods concentrate on assessing speckle suppression and edge information retention capabilities.

A. Speckle Suppression Evaluation Methods

The ENL serves as a measure of the speckle-smoothing ability within a homogeneous patch of an image and can be expressed as follows:

$$\mathrm{ENL} = \frac{\mu(F_{\mathrm{HR}})^2}{\mathrm{Var}(F_{\mathrm{HR}})} \tag{1}$$

where F_{HR} represents the homogeneous patch of the filtered image; and μ and Var denote the mean and variance of the image, respectively. The ENL value is positively correlated with the smoothness of the homogeneous patch. However, ENL values may prove unreliable for patches with poor mean-preserving properties.

The SMPI effectively addresses the limitation of ENL stability by quantifying the mean difference between images before and after filtering, given by

$$\mathrm{SMPI} = (1 + |\mu_{N_{\mathrm{HR}}} - \mu_{F_{\mathrm{HR}}}|) \cdot \frac{\sigma(F_{\mathrm{HR}})}{\sigma(N_{\mathrm{HR}})} \tag{2}$$

where N_{HR} represents the homogeneous patch of the speckled image; $\sigma(N_{\mathrm{HR}})$ and $\sigma(F_{\mathrm{HR}})$ denote the standard deviations of the image within the homogeneous patch before and after filtering, respectively. A lower SMPI value indicates superior filtering performance in terms of mean preservation and speckle reduction.

The coherent equivalent number of looks (CENL) [4] characterizes the speckle suppression performance of a filter by establishing a correlation between the speckled and ratio images. CENL uses weighted Euclidean distance between pixel blocks to select homogeneous patches, reducing the need for manual patch selection time. It is defined as follows:

$$\mathrm{CENL} = k * (1 - \mathrm{CC}(F_{\mathrm{HR}}, R_{\mathrm{HR}})) + \frac{1}{\log 10(\mathrm{MENL})} \tag{3}$$

$$\mathrm{MENL} = \frac{1}{n_{\mathrm{HR}}} \sum_{i_{\mathrm{HR}}=1}^{n_{\mathrm{HR}}} \mathrm{ENL}(F_{i_{\mathrm{HR}}}) \tag{4}$$

where MENL represents the mean ENL for extracting patches, k is a constant ensuring equal magnitudes in both parts, $\mathrm{CC}(F_{\mathrm{HR}}, R_{\mathrm{HR}})$ denotes the correlation coefficient between the speckled image and the ratio image, which is composed of the ratio of the original image to the filtered image, and i_{HR} signifies the i th homogeneous patch and n_{HR} represents the total number of extracted homogeneous patches. The CENL value falls within the domain of [0, 1], with closer proximity to 0 indicating superior speckle-smoothing effects of the filter.

B. Edge Retention Evaluation Methods

The ESI is a measure of the filter's ability to maintain edges in the horizontal and vertical directions. The specific expression

is given as follows:

$$\mathrm{ESI} = \frac{\sum_{i,j\in\Omega}\sqrt{H(F)^2 + V(F)^2}}{\sum_{i,j\in\Omega}\sqrt{H(N)^2 + V(N)^2}} \tag{5}$$

where Ω denotes the domain image; i and j represent the pixel positions, respectively; *N* and *F* represent the speckled image and filtered image, respectively; *H* and *V* denote the horizontal and vertical directions, respectively; the calculation formulae for images *I*, *H*, and *V* are as follows: $H(I) = I(i,j) - I(i+1,j)$, $V(I) = I(i,j) - I(i,j+1)$, and higher ESI values indicate a better filter edge retention performance.

The SSIM is a measure of the similarity between two images, primarily evaluating image brightness, contrast, and structure to construct a comprehensive assessment of image structure information. The model is expressed as follows:

$$\mathrm{SSIM} = \frac{2\mu_N\mu_F + C_1}{{\mu_N}^2 + {\mu_F}^2 + C_1} \cdot \frac{2\sigma_{N,F} + C_2}{{\sigma_N}^2 + {\sigma_F}^2 + C_2} \tag{6}$$

where C_1 and C_2 are the constants used to avoid situations where the numerator and denominator are 0. They can be calculated using the following equation: $C_1 = (K_1 \cdot L)^2$ and $C_2 = (K_2 \cdot L)^2$, where K_1 and K_2 are very small constants, and L represents the dynamic range of pixel values; and μ_N, μ_F, σ_N, and σ_F denote the mean and standard deviation of the images before and after filtering, respectively. $\sigma_{N,F}$ represents the covariance matrix between the speckle image and the filtered image. The SSIM takes a value in the range of [0, 1]; the closer the value is to 1, the more similar the structural information of the two images.

C. Integrated Evaluation Methods

The *M*-index combines the deviation of the residual structure of the ratio image from its statistical properties for a comprehensive assessment of image denoising performance. It is expressed as follows:

$$M = r_{\mathrm{E\hat{N}L},\hat{\mu}} + \delta h \tag{7}$$

where $r_{\mathrm{E\hat{N}L},\hat{\mu}}$ represents the first-order residuals of the n regions and is modeled as follows:

$$r_{\mathrm{E\hat{N}L},\hat{\mu}} = \frac{1}{2}\sum_{i=1}^{n_{\mathrm{HR}}}\left(r_{\mathrm{E\hat{N}L}}(i) + r_{\hat{\mu}}(i)\right) \tag{8}$$

where $r_{\mathrm{E\hat{N}L}(j)} = [\mathrm{E\hat{N}L}_N(j) - \mathrm{E\hat{N}L}_R(j)]/\mathrm{E\hat{N}L}_N(j)$ denotes the relative residuals resulting from the deviation from the ideal ENL value; $\mathrm{E\hat{N}L}_N(j)$ and $\mathrm{E\hat{N}L}_R(j)$ denote the ENLs of the noisy and ratio images in the homogeneous patch, respectively. $r_{\hat{\mu}}(i) = |1 - \hat{\mu}_R(i)|$ represents the degree of deviation between the mean value of the ratio image and the ideal value. δh is calculated as follows:

$$\delta h = 100\,|h_o - h_g|\,/h_o \tag{9}$$

where h denotes the inverse difference moment component of the grayscale covariance matrix, modeled as follows:

$$h = \sum_i\sum_j \frac{1}{1 + (i-j)^2} \cdot p(i,j) \tag{10}$$

where $p(i,j)$ denotes the normalized grayscale covariance matrix at (i,j), and h_o and h_g denote the mean values of the original ratio image and ratio image with texture information transformation, respectively. The size of the *M* metric is inversely proportional to the filtering performance, i.e., the smaller the value of *M*, the better the filtering performance.

III. Proposed Despeckling Image Quality Evaluation Method

A novel IQE_HHSP is proposed. The overall process is illustrated in Fig. 1. First, an adaptive method for extracting homogeneous and heterogeneous scene patches was established based on noisy images combined with grayscale features to achieve the precise extraction of homogeneous and heterogeneous patches. The homogeneous evaluation factor (HoEF) was constructed by combining the fuzzy index with the gradient difference and speckle suppression index (GDSSI). Subsequently, a heterogeneous evaluation factor (HeEF) was constructed by integrating the amplitude, global, and local feature change information. Finally, the proposed IQE_HHSP index was constructed using HoEF and HeEF in a comprehensive evaluation model.

A. Adaptive Extraction of Homogeneity and Heterogeneity Scene Patches

The core objective of the filtered image evaluation task is to effectively assess the speckle-smoothing capability in homogeneous patches and the ability to retain detailed information in heterogeneous patches. Hence, it is imperative to accurately extract homogeneous and heterogeneous patches for evaluation purposes. Currently, homogeneous patches are predominantly selected manually, while automatic extraction methods mainly concentrate on homogeneous patches, neglecting research on heterogeneous patch extraction [4], [34], [35], [36], [37]. In light of this, we propose an adaptive extraction method for homogeneous and heterogeneous scene patches utilizing the maximum residual structure and gradient change model (MRSGCM).

The fundamental distinction between homogeneous and heterogeneous scenes lies in the uniformity of pixel information within the scene. Theoretically, pixel values remain consistent in homogeneous scenes [4], [36]. However, actual homogeneous scenes exhibit inconsistencies in pixel information due to speckle interference. Pixel variations in homogeneous scenes are notably lower compared with those in heterogeneous scenes. Figs. 2 and 3 present the magnified display and statistical outcomes of the selected GF-3 homogeneous and heterogeneous patch, respectively, further affirming that the amplitude difference in pixel values within homogeneous patch is significantly smaller than that within heterogeneous patch. Heterogeneous patches tend to exhibit steeper pixel slopes. Thus, distinguishing between homogeneous and heterogeneous patches can be

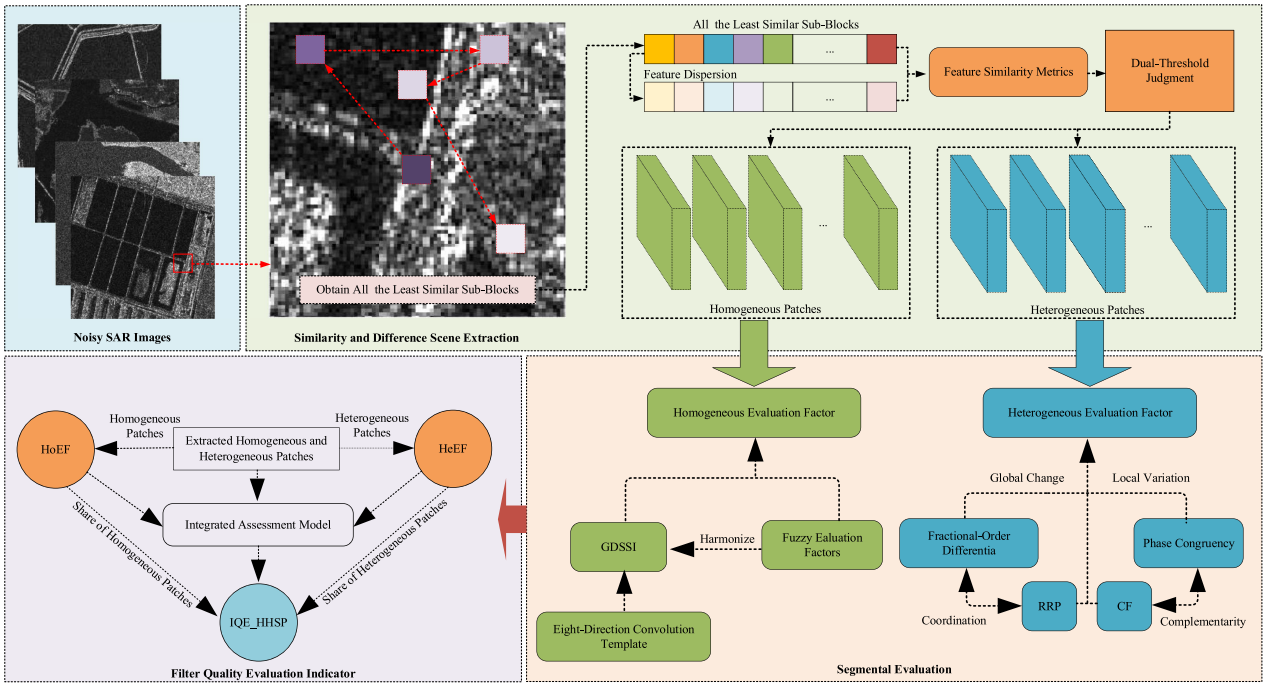

Fig. 1. Overall process of the methodology presented in this article.

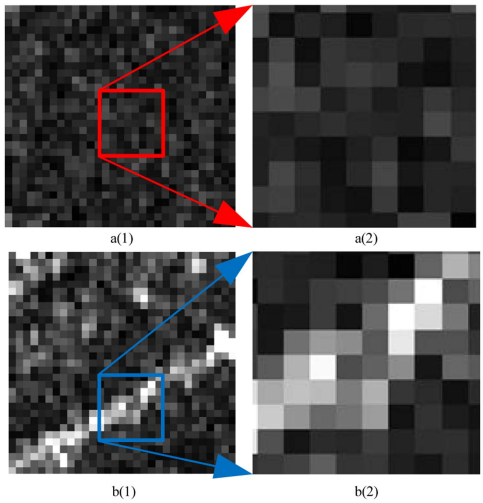

Fig. 2. Enlarged display of (a) homogeneous and (b) heterogeneous patches.

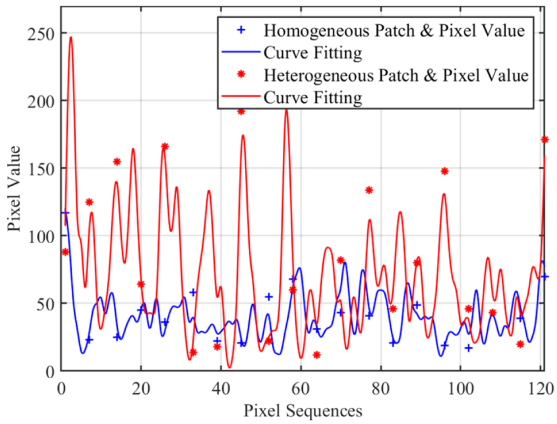

Fig. 3. Homogeneous and heterogeneous patches pixel statistics' results.

accomplished by analyzing pixel difference information within the scene.

However, distinguishing homogeneous and heterogeneous patches directly using only the pixel difference feature is challenging; thus, a method of seeking the maximum dissimilarity sub-block through iterative gradient changes is proposed. Initially, the gradient magnitudes of the central and neighboring sub-blocks were computed, and similarity was assessed by constructing the gradient difference eigenfunction. The model is represented as follows:

$$\mathrm{GSM}_{\mathrm{CO}}^{K} = e^{-\frac{1}{mn}\sqrt{\sum\left(\mathrm{GM}\left(I_{\mathrm{CO}}^{K}\right)-\mathrm{GM}(I_{\delta})\right)^{2}}}, \delta \in I \tag{11}$$

where m and n represent the ranks of the matrix blocks; I represents the patch of being discriminated; I_{CO} and I_{δ} represent the center sub-block and the neighborhood sub-block of I, respectively; GM represents the gradient magnitude; K represents the number of iterations; Σ represents summing by pixel position, and $\mathrm{GSM}_{\mathrm{CO}}^{K}$ represents the gradient similarity matrix between the center sub-block and the neighbor sub-block of K iterations. When K is 1, the default matrix geometric center sub-block is the center sub-block, and when K is not 1, the center sub-block is calculated as follows:

$$\begin{cases} I_{\mathrm{CO}}^{K+1} = \min\{GSM_{\mathrm{CO}}^{K}, \delta \in I\} & \text{(a)} \\ I_{\mathrm{CO}}^{K+1} \neq I_{\mathrm{CO}}^{K}. & \text{(b)} \end{cases} \tag{12}$$

The central sub-block obtained based on (12)-(a) acts again on (11), and under the condition of satisfying (12)-(b), the different

maximum dissimilarity matrix block (MDMB) is calculated as follows:

$$\mathrm{MDMB} = \left\{ I_{\mathrm{CO}}^{1}, I_{\mathrm{CO}}^{2}, \ldots, I_{\mathrm{CO}}^{K}, \ldots, I_{\mathrm{CO}}^{t} \right\} \tag{13}$$

where t signifies the maximum number of dissimilar sub-blocks acquired from the final iteration. The geometric content of the MDMB is evaluated using the inverse difference moments of the grayscale covariance matrix. The inverse difference moment gauges the degree of texture variation in the image, with higher values indicating increased local homogeneity [42]. The specific formula is provided by (10).

Combining the maximum dissimilar sub-block MDMB with the MDMB version obtained by changing its texture information order, the corresponding inverse difference moment values τ and τ' are calculated using (10). The final matrix block adaptive differentiation factor was obtained by combining the structural feature metric models as follows:

$$f_I = \left| \log \left(1 - \frac{\mu(\tau + \tau')}{\mathrm{SC}(\tau, \tau')} \right) \right| \tag{14}$$

where f_I denotes the adaptive differentiation factor of the patch I and SC denotes the similarity criterion, which is modeled as follows:

$$\mathrm{SC}(A, B) = \frac{A}{B} + \frac{B}{A}. \tag{15}$$

According to (15), the homogeneous and heterogeneous patch discriminant factor can be calculated for each block of the matrix to be discriminated. The value of f_I ranges between [0, 1], and the larger the value of f_I, the higher the possibility of homogeneous patches; the smaller the value, the higher the possibility of heterogeneous patches. To ensure the accuracy of the discrimination between homogeneous and heterogeneous patches, this article takes the gradient matrix obtained in (11), the central sub-block gradient (taking the central sub-block at $K = 1$), and its neighboring sub-block Euclidean distance and obtains the second control factor f_I' using the gradient difference feature model, which is stated as follows:

$$f_I' = \exp\left(- \frac{\sum \sqrt{\left(\mathrm{GM}_{\mathrm{CO}}^{K=1} - \mathrm{GM}_{\delta}^{K=1} \right)^2}}{h'} \right) \tag{16}$$

where h' is the control factor, which defaults to a constant value to control the range of f_I' within a reasonable range. Therefore, homogeneous and heterogeneous patches can be effectively differentiated by setting suitable threshold values. The specific setting method was given as follows:

$$\mathrm{DF}_i = \begin{cases} 1 & f_I > T1 \text{ and } f_I' > H1 \\ 0 & f_I < T2 \text{ and } f_I' > H2 \end{cases} \tag{17}$$

where DF_i represents the homogeneity discriminant factor of the i th patch, and 1 and 0 represent the homogeneous and heterogeneous patches, respectively. The extraction of homogeneous and heterogeneous patches of an image can be effectively realized using the above steps. However, the extraction of homogeneous and heterogeneous patches is only used for subsequent evaluations; therefore, it is unnecessary to accurately extract every homogeneous and heterogeneous patch. To ensure the reliability of the selected patches of homogeneity and heterogeneity, $T1$, $T2$, $H1$, $H2$, and h' were generally set to 0.95, 0.8, 0.9, 0.1, and 10, respectively, and the default patch size is 30×30.

B. Gradient Differences and Speckle Suppression Indicators

Traditional ENL and SSI are ineffective in distinguishing between effective speckle suppression and oversmoothing phenomena when evaluating filtering model performance [36], [37]. SMPI and MPSSI have improved ENL and SSI, effectively mitigating the impact of mean value index differences on speckle smoothing. However, this article introduces edge model-based blur metric (EMBM) fuzzy metrics and proposes GDSSIs due to the limitations of SMPI and MPSSI of using the mean value as an intrinsic index for disparity metrics and resolution reduction of the filtered image. Readers can find specific details about EMBM in [3].

Sobel edge detection [47] demonstrates good edge-smoothing performance and is the most used first-order edge detection algorithm for optical images. However, the Sobel operator typically considers only horizontal and vertical gradients in the convolution template, which may not capture actual edges accurately. Therefore, this study employs an eight-direction convolution template for improved edge detection and applies its results to edge detection in SAR images. The convolution template is illustrated in Fig. 4.

The homogeneous patches derived from the filtered image using the MRSGCM method were convolved with the template described above, as per (18), to generate the gradient magnitude image and identify the maximum gradient magnitude, as follows:

$$\begin{cases} \mathrm{GM}_{j,i} = M_i \otimes \mathrm{HR}_j \\ \mathrm{MGM}_j = \max\left\{ \sqrt{\sum_i \mathrm{GM}_{j,i}^2} \right\} \end{cases} \quad (1 \le i \le 8) \tag{18}$$

where HR_j denotes the j th homogeneous patch; M_i represents the i th directional template mentioned above; $\otimes$ represents the convolution operation; and MGM_j denotes the maximum gradient of the j th homogeneous patch. The amplitude was used to construct the GDSSI, and the specific model was as follows:

$$\mathrm{GDSSI} = \left(1 - \frac{\mathrm{MGM}_{F(j)}}{\mathrm{MGM}_{N(j)}} \right) \left| \log\left(\frac{s_F}{s_N} \right) \right| \tag{19}$$

where F and N represent the filtered and speckle images, respectively; and $\mathrm{MGM}_{F(j)}$ and $\mathrm{MGM}_{N(j)}$ represent the maximum gradients of the j th homogeneous patch in the filtered image and the speckle image, respectively. A larger value of GDSSI indicates that the filter is more effective in speckle suppression. For the blur evaluation of the image, this study adopted the EMBM indicator [3], which evaluates the width and contrast of the edge pixels, utilizes saliency edges to mimic the blur evaluation of the human visual system (HVS), and ultimately passes the cumulative probability of blur detection [48] metric to obtain the final blur quality score. Higher EMBM values result in clearer corresponding images. The specific indicator model

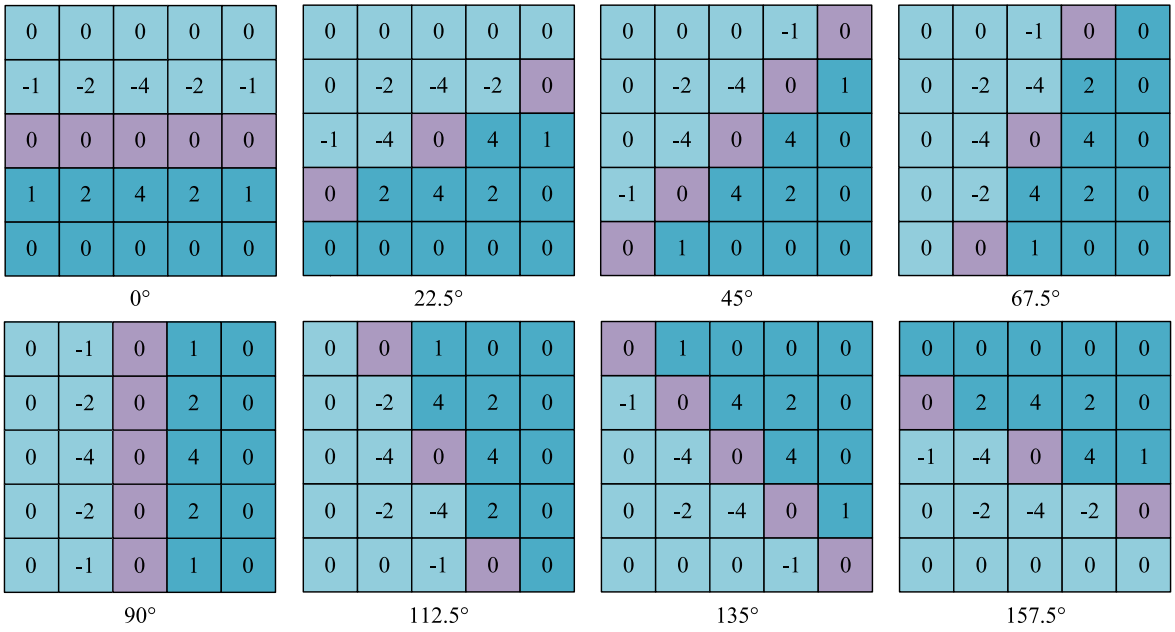

Fig. 4. Eight-direction convolutional template.

of EMBM is given as follows:

$$\mathrm{EMBM} = P\left(P_{\mathrm{BLUR}} \le P_{\mathrm{JNB}}\right) = \sum_{P_{\mathrm{BLUR}}=0}^{P_{\mathrm{BLUR}}=P_{\mathrm{JNB}}} P\left(P_{\mathrm{BLUR}}\right) \quad (20)$$

where JNB represents the fuzzy standard deviation; P_{BLUR} represents the blur probability of each edge pixel; and P_{JNB} represents the minimum blur probability that can be detected by HVS exactly. The details about (20) can be found in [3] and [48]. The blur evaluation index should be based on speckle suppression; therefore, it should receive a lower weight when the SSI is low

$$W = K \cdot \mathrm{GDSSI} \quad (21)$$

where *K* represents the weight, with a range of values between [0, 1] in order to reduce the weight of fuzzy indicator. Combining the above indicators to obtain the final homogeneous-area evaluation factor, the larger the value, the better the performance of speckle smoothing. The model is given as follows:

$$\mathrm{HoEF} = \mathrm{GDSSI} + W \cdot \mathrm{EMBM}_F. \quad (22)$$

C. Indicators to Assess Heterogeneous Patches

The texture of heterogeneous patches is more complex than that of homogeneous patches, making it challenging to accurately characterize their texture and structural characteristics. In light of this, this study aimed to track the texture change features of heterogeneous patches from both global and local perspectives.

1) Global Feature Difference Model (GFDM) of Heterogeneous Patches: Fractional-order differentiation, an extension of integer-order differentiation, possesses features, such as short-term memory, which can effectively characterize global properties and has found applications in measuring global changes in images within the field of image processing. Another characteristic used for image description of global change is radiation retention performance (RRP), which is another characteristic that distinguishes SAR from optical images. Building upon these concepts, a global feature model of heterogeneous patches was proposed, employing fractional-order differentiation combined with RRP.

Grünwald – Letnikov (GL) [49], [50] is a popular and commonly used definition in fractional-order differentiation methods. The αth fractional derivative of 2-D signal was defined as follows:

$$D_H^{\alpha} x_i = \begin{pmatrix} \frac{x_{i1}}{h^{\alpha}}, \frac{-\Gamma(\alpha+1)x_{i1}}{h^{\alpha}\Gamma(2)\Gamma(\alpha)} + \frac{x_{i2}}{h^{\alpha}}, \ldots, \\ \frac{(-1)^{n-1}\Gamma(\alpha+1)x_{i1}}{h^{\alpha}\Gamma((n-1)+1)\Gamma(\alpha-(n-1)+1)} \\ + \cdots + \frac{-\Gamma(\alpha+1)x_{i(n-1)}}{h^{\alpha}\Gamma(2)\Gamma(\alpha)} + \frac{x_{in}}{h^{\alpha}} \end{pmatrix} \quad (23)$$

where h is the increment of the independent variable. For the ith line x_i of the image, $x_i = (x_{i1}, x_{i2}, \ldots, x_{iN})$; Γ represents the gamma function; *n* denotes the number of columns of the matrix; and *H* denotes the horizontal direction. Similarly, the fractional-order differential $D_V^{\alpha} y_j$ of the 2-D signal in the jth column can be obtained. On this basis, the fractional-order differential matrices D_H^{α} and D_V^{α} of the whole image in the horizontal and vertical directions are obtained.

Eventually, the GL matrices corresponding to the 2-D image are defined by D_H^{α} and D_V^{α} as follows:

$$\mathrm{GL} = \sqrt{\left(D_H^{\alpha}\right)^2 + \left(D_V^{\alpha}\right)^2}. \quad (24)$$

By using the GL matrix, we can effectively observe the global variation characteristics of SAR images before and after filtering.

The RRP reflects the radiation changes in the image before and after filtering, and the specific model is given as follows:

$$\mathrm{RRP} = \frac{\mu_N}{\mu_F}. \tag{25}$$

Using the GL and RRP matrices, we can analyze the global feature changes in both horizontal and vertical directions of the heterogeneous images. Ideally, for perfectly filtered images, we expect minimal differences in the global feature changes of heterogeneous patches before and after filtering. Therefore, we propose a GFDM as follows:

$$\mathrm{GFDM} = \exp\left(-\frac{1}{m \cdot n}\sum_{i\in\Omega}\left(\frac{\mathrm{GL}_N}{\mathrm{GL}_F} + \frac{\mathrm{GL}_F}{\mathrm{GL}_N}\right)\right) \cdot \mathrm{RRP} \tag{26}$$

where m and n denote the number of rows and columns of the image, respectively, i represents the pixel position, and Ω represents the image domain. The range of GFDM values is between 0 and 1; higher values indicate smaller global feature differences between the image before and after filtering.

2) Local Features Model of Heterogeneous Patches: Phase consistency (PC) [51] serves as a vital metric for local image features, with high PC indicating the presence of rich edge information in frequency-domain images. Given that the HVS primarily perceives images through low-level features, such as edges, PC can be viewed as a simulation of the HVS in heterogeneous patches. It can be formulated as follows:

$$\mathrm{PC}_{2\mathrm{D}}(x) = \frac{\sum_{j=1}^{J}\sqrt{F_{\theta_j}^2(x) + H_{\theta_j}^2(x)}}{\varepsilon + \sum_n \sum_j A_{n,\theta_j}(x)} \tag{27}$$

where $\mathrm{PC}_{2\mathrm{D}}$ denotes the 2-D PC; x denotes the position; θ_j denotes the filter direction angle; J is the number of all direction angles, ε is a constant; A_n is the local amplitude at scale n, which can be modeled as $A_n(x) = \sqrt{e_n(x)^2 + o_n(x)^2}$, where e_n and o_n, respectively, represent the response of scale n even symmetric and odd symmetric filters; A_{n,θ_j} represents the amplitude in scale n and direction θ_j; and $F(x)$ and $H(x)$ can be modeled as $F(x) = \sum_n e_n(x)$ and $H(x) = \sum_n o_n(x)$. For more theoretical knowledge about PC, readers can find it in [51].

The PC value domain is [0, 1]. However, the local contrast of the image can affect the visual effect, owing to the relative invariance of the PC to changes in image contrast; therefore, it is necessary to use contrast features (CFs) for compensation. The CF reflects the variation in the backscatter coefficient of the SAR images. The model is given as follows:

$$\mathrm{CF} = \frac{\max(I) - \min(I)}{\max(I) + \min(I)} \tag{28}$$

where max(I) and min(I) represent the maximum and minimum pixel values of the image I, respectively. The PC and CF play complementary roles in characterizing the local quality of an image.

Using PC and CF, the local variation characteristics of the heterogeneous patches can be obtained. Better filtering models should exhibit small local variation differences between the images before and after filtering. Therefore, a local feature difference model (LFDM) was proposed

$$\mathrm{LFDM} = \frac{\sum_{p_i}(\mathrm{PC}_N \cdot \mathrm{PC}_F)}{\sum_{p_i}(\mathrm{PC}_F^2 + \mathrm{PC}_N^2)} \cdot \frac{\mathrm{CF}_F}{\mathrm{CF}_N} \tag{29}$$

where p_i represents each pixel point. The range of the LFDM values was [0, 1], and there was a small local difference in the image before and after filtering, which was linked to a larger LFDM value.

3) Heterogeneous Evaluation Factor: By combining the global and local metrics, the final comprehensive assessment metrics for heterogeneous patches were obtained, and the specific model was described as follows:

$$\mathrm{HeEF} = 1 - \exp\left\{-\sqrt{\sum_{\mathrm{HeP}}(\mathrm{HPDM}(N,F))}\right\} \tag{30}$$

where HeP represents the extracted homogeneous patches; and HPDM represents the difference model between speckle images and filtered images in heterogeneous patches

$$\mathrm{HPDM}(N,F) = \mathrm{GFDM} \cdot \mathrm{LFDM}. \tag{31}$$

The range of the HeEF values was [0, 1]. As HeEF approaches 1, the filtering model can extract richer information from the heterogeneous patches.

D. Proposed IQE_HHSP Evaluation Model

The proposed IQE_HHSP metric combines HoEF and HeEFs and provides an overall assessment of speckle suppression and information retention. The model is given as follows:

$$\mathrm{IQE\_HHSP} = C\left(\mathrm{HoEF}/\lambda_\Omega^{\mathrm{HoP}} + \mathrm{HeEF}/\lambda_\Omega^{\mathrm{HeP}}\right)^{\frac{\sum \mathrm{EP}}{\sum \mathrm{BS}}} \tag{32}$$

where $\sum$EP denotes the sum of homogeneous and heterogeneous patches extracted; C is a constant to control the output range; $\lambda_\Omega^{\mathrm{HoP}}$ and $\lambda_\Omega^{\mathrm{HeP}}$ denote the number of extracted homogeneous and heterogeneous patches of image domain Ω, respectively; and $\sum$BS represents the sum of sub-blocks that the original image is divided into. A perfect filtering model should exhibit larger values in the IQE_HHSP metrics, and a smaller IQE_HHSP indicates that the performance of the filter is far from the ideal value.

As a whole, the detailed process of the proposed evaluation indicators is given as follows:

Validation experiments on the IQE_HHSP metric were then conducted to demonstrate that the results have a better match with the HVS.

IV. Experiments and Analysis

This section applies the proposed metrics to evaluate the quality of the SAR filtering model. One simulated SAR image and four SAR images were selected for the experiment (see Fig. 5), and the specific parameters of SAR images are listed in Table I. The simulated image, as shown in Fig. 3(a), is synthesized by adding multiplicative speckle to a clean environment. The corresponding data source can be found in [3]. The filtering models included EnLee [7], NLM [22], PPB [26], FANS [25],

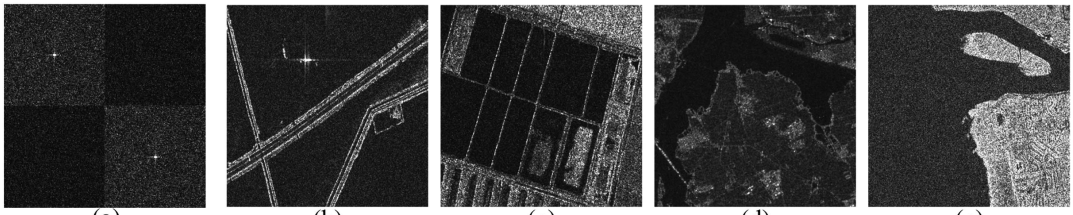

Fig. 5. Display of five test images. (a) Simulated SAR. (b) GF-3. (c) TerraSAR-X. (d) Sentinel-1. (e) Radarsat-2.

Algorithm 1: IQE_HHSP.

Procedure

- Step 1: For SAR image I, extracting HoP and HeP based on (11)–(17)
- Step 2: Calculate the HoEF index for the extracted HoP:
  1) Calculate GDSSI based on (18) and (19)
  2) Obtaining fuzzy indicator EMBM based on (20)
  3) Calculate fuzzy weights and obtain HoEF index based on (21) and (22)
- Step 3: Calculate the HeEF index for the extracted HeP:
  1) Construct GFDM and calculate GFDM based on (25) and (26)
  2) Construct LFDM and calculate LFDM based on (28) and (29)
  3) Output HeEF index based on (30) and (31)
- Step 4: Combining HoEF and HeEF indicators to obtain IQE_HHSP index through (32)

End Procedure

SRAD [17], and SARBM3D [24]. Evaluation metrics comprised speckle suppression indices (ENL, SMPI, and CENL), edge retention indices (ESI, SSIM, and DPI), and the comprehensive evaluation index (M).

For all experiments, the parameter set of the filtering model mentioned above is based on the default parameter provided by the authors of the corresponding reference article. In the adaptive homogeneous and heterogeneous patch selection experiments, the threshold parameters defaulted to $T1 = 0.95$, $T2 = 0.8$, $H1 = 0.9$, and $H2 = 0.1$. The default setting of the weight K in the evaluation of homogeneous patches is 0.2. In the evaluation of heterogeneous patches' experiments, following the literature, the fractional successive differentiation of order $\alpha = 0.6$ was selected, and $h = 80$. This experiment is programmed using MATLAB, with a processor model of i9-12900, a memory size of 128 GB, and a 1 TB hard disk capacity.

A. Experiments on Homogeneous and Heterogeneous Patch Extraction

Experiments were conducted for the extraction of homogeneous and heterogeneous SAR image patches first. The structural residual information of the image was extracted using the model proposed in (10)–(16), and homogeneous and heterogeneous patches were extracted based on the threshold set in (17), respectively. The experimental analysis is presented in Fig. 6, and the numbers of extracted homogeneous and heterogeneous patches of test images are listed in Table II.

The proposed MRSGCM method effectively distinguishes dissimilar patches and accurately extracts them (see Fig. 6 and Table II). The number of extractions also provides sufficient data support for subsequent evaluation experiments.

B. Evaluation Experiments of the Simulated SAR Image Filtering Models

The filtered images and local zoomed-in areas of the simulated SAR image are displayed in Fig. 7. Corresponding metrics evaluation results and rankings are shown in Table III, where the metric evaluation rankings are marked in bold.

Visually, the six filtering models effectively suppress coherent speckle. While FANS and SARBM3D do not exhibit notably strong speckle suppression, their capacity to preserve edge information surpasses that of the other four techniques. Conversely, NLM and SRAD, despite their more pronounced speckle reduction, suffer from significant blurring and loss of edge details. PPB is characterized by a noticeable pseudotexturing phenomenon, which impairs its effectiveness in both edge preservation and speckle suppression, thus not distinguishing it as superior in these areas.

Quantitatively, the proposed HoEF maintains good consistency with traditional ENL and CENL. The rationale behind the HoEF index's assertion that speckle suppression of EnLee outperforms PPB lies in the latter's pronounced pseudotexturing, which causes notable discrepancies within homogeneous patches. The remaining indicators of HoEF match the visual results. In the realm of edge-preservation assessment, HeEF and ESI demonstrate a strong concurrence, with both metrics affirming that SARBM3D and FANS excel in retaining essential image details. In contrast, NLM and SRAD are observed to suffer from a more substantial loss of information. The pseudotexturing generated by PPB makes it not dominant in the HeEF index. According to the IQE_HHSP index, both NLM and SRAD have garnered low scores. The primary reason for this outcome is the increased edge loss and blurring caused by NLM and SRAD, which significantly contribute to their subpar performance. FANS and SARBM3D secured the top and runner-up positions, respectively, owing to their adeptness at mitigating speckle while concurrently retaining a substantial amount of edge details. However, the assertion that the M index

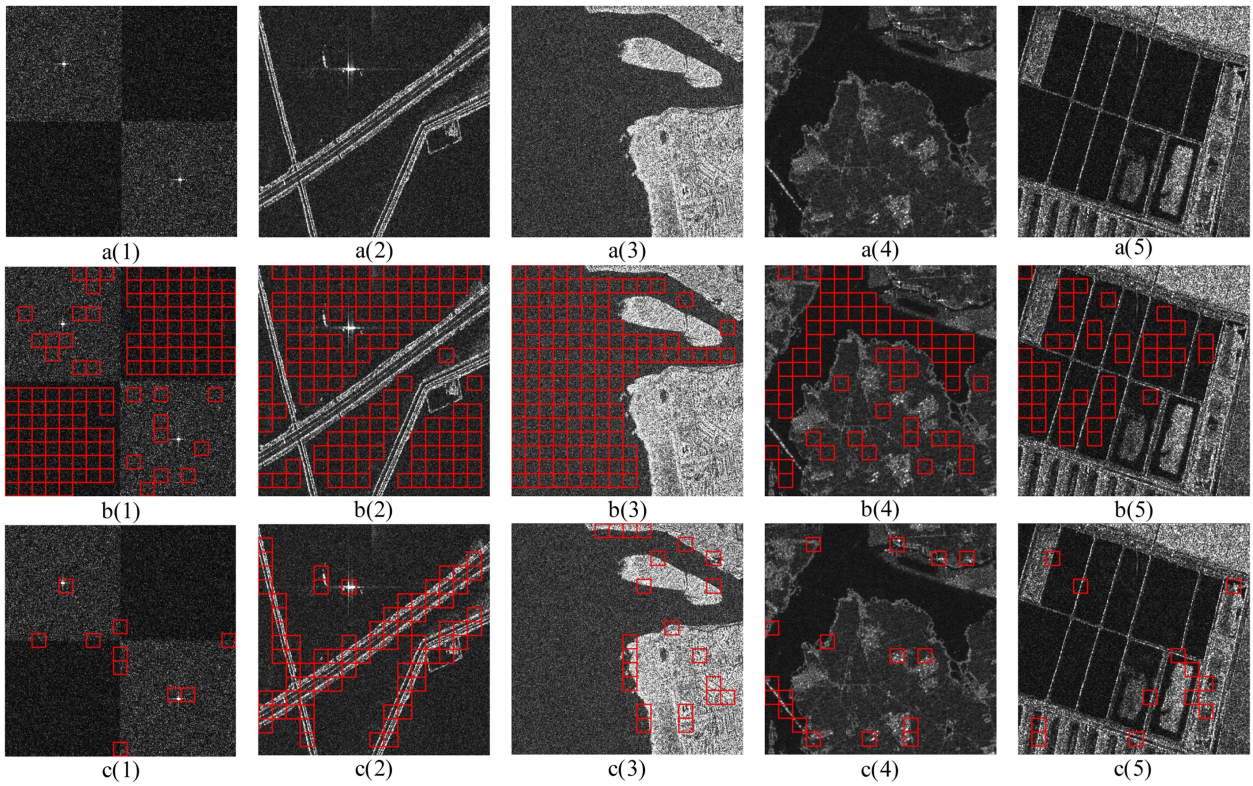

Fig. 6. a(1) Simulated SAR. a(2) GF-3. a(3) TerraSAR-X. a(4) Sentinel-1. a(5) Radarsat-2. b(1)–(5) are the adaptively extracted homogeneous patches. c(1)–(5) are the adaptively extracted heterogeneous patches.

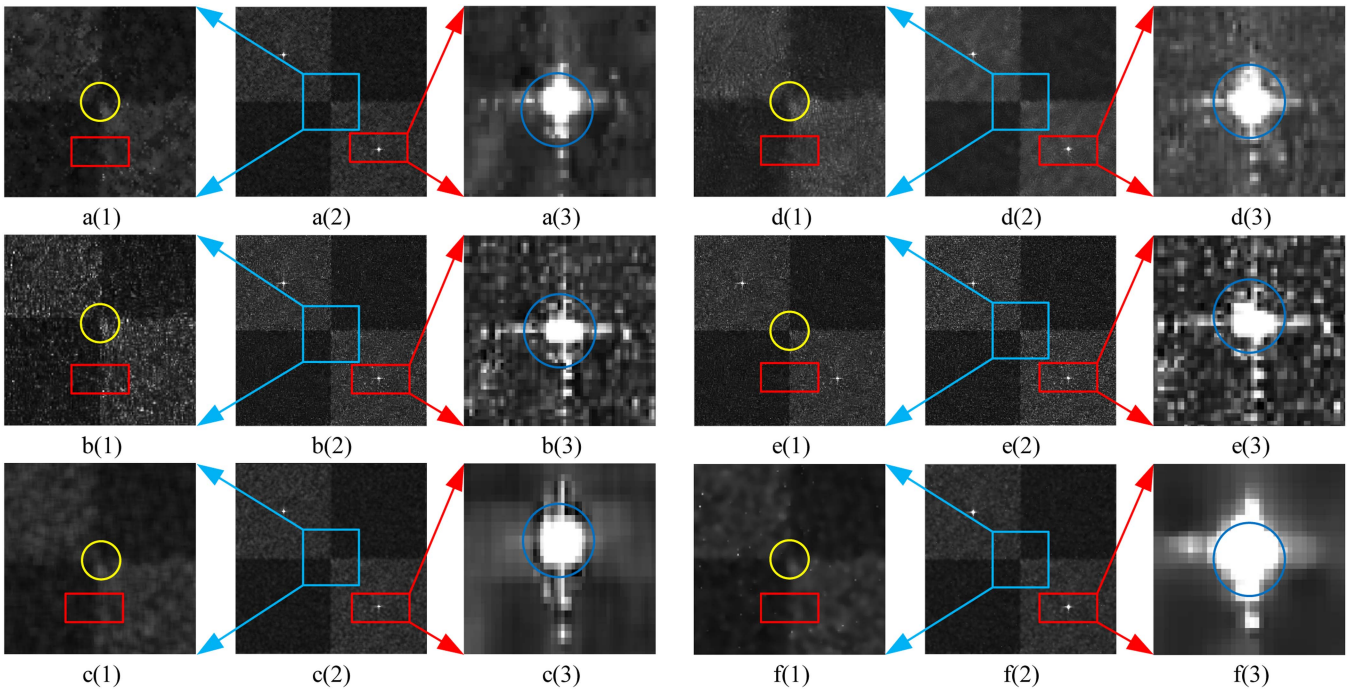

Fig. 7. Filtered simulated SAR image by a(2) EnLee, b(2) FANS, c(2) NLM, d(2) PPB, e(2) SARBM3D, and f(2) SRAD. The first, third, fourth, and sixth columns are zoomed-in displays of the corresponding filters, respectively.

TABLE I
SAR IMAGES RELATED PARAMETERS

Sensors	Band	Polarize	Resolution	Date	Region
GF-3	C	VV	3m	2017-02-24	Tianjin, China
Radarsat-2	C	HV	8m	2008-04-19	Vancouver, Canada
TerraSAR-X	X	HH	3m	2010-03-08	Tianjin, China
Sentinel-1	C	VH	5m	2023-04-19	Bengbu, China

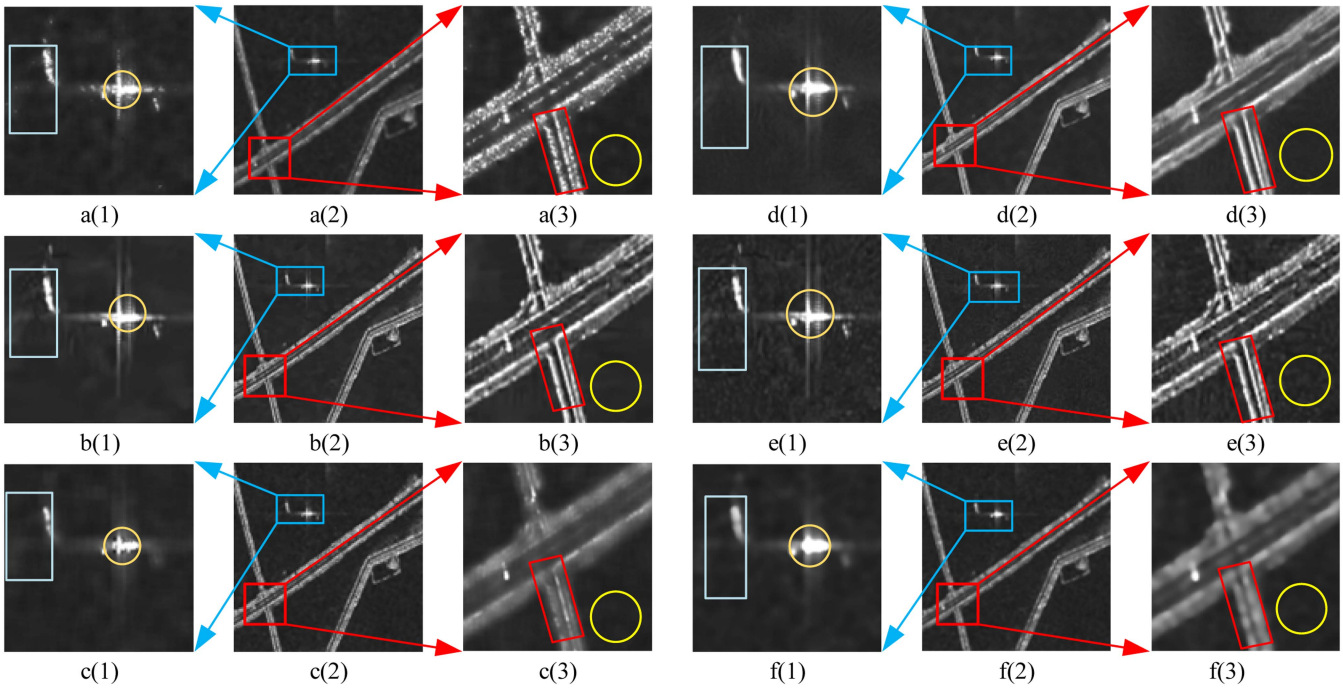

Fig. 8. Filtered GF-3 SAR image by a(2) EnLee, b(2) FANS, c(2) NLM, d(2) PPB, e(2) SARBM3D, and f(2) SRAD. The first, third, fourth, and sixth columns are zoomed-in displays of the corresponding filters, respectively.

TABLE II
NUMBER OF HOMOGENEOUS AND HETEROGENEOUS PATCHES EXTRACTED

Sensors	Number of homogeneous patches	Number of heterogeneous patches
Simulated SAR	129	10
GF-3	163	73
Radarsat-2	140	22
TerraSAR-X	44	12
Sentinel-1	64	17

demonstrates SRADs superior filtering performance remains unconvincingly supported within the scope of this experimental framework.

Overall, the IQE_HHSP index is basically consistent with the visual results, verifying its effectiveness in evaluating the filtering of simulated SAR images.

C. Evaluation Experiments of the GF-3 Image Filtering Models

The filtered images and local zoomed-in areas of the GF-3 images are displayed in Fig. 8. Corresponding metrics evaluation results and rankings are shown in Table IV, where the metric evaluation rankings are marked in bold.

Visually, the six methods mentioned above effectively smoothed the speckle. However, the filtered images by SRAD and EnLee methods exhibited significant oversmoothing. The undersmoothing phenomenon of SARBM3D was particularly evident. FANS, PPB, and NLM demonstrated better overall smoothing effects, with PPB being slightly less smooth than FANS but better than NLM. In terms of edge preservation, SARBM3D preserved the most abundant edge information, followed by FANS and PPB. NLM and SRAD resulted in relatively severe edge losses, while EnLee exhibited certain edge loss and local strong pixel points.

Quantitatively, the proposed HoEF achieves the same conclusions as traditional ENL and CENL methods in all filtering model evaluations. SRAD showed a more severe oversmoothing

TABLE III
ASSESSMENT METRICS AND RANKING FOR THE SIMULATED SAR IMAGE

Filters	ENL	SMPI	CENL	ESI	SSIM	HoEF	HeEF	M	IQE_HHSP
EnLee	20.00/**4**	13.32/**3**	0.77/**4**	0.22/**4**	0.93/**1**	1.15/**3**	0.37/**3**	17.71/**3**	1.88/**3**
FANS	3.96/**5**	15.33/**6**	1.68/**5**	0.69/**2**	0.89/**5**	0.27/**5**	0.51/**2**	113.95/**5**	2.11/**1**
NLM	39.63/**2**	14.43/**4**	0.63/**2**	0.17/**5**	0.93/**2**	1.59/**1**	0.30/**5**	8.75/**2**	1.79/**5**
PPB	28.20/**3**	10.37/**2**	0.69/**3**	0.33/**3**	0.87/**6**	0.98/**4**	0.35/**4**	36.22/**4**	1.81/**4**
SARBM3D	2.21/**6**	14.82/**5**	2.90/**6**	0.75/**1**	0.90/**4**	0.21/**6**	0.55/**1**	234.14/**6**	2.10/**2**
SRAD	47.29/**1**	8.39 /**1**	0.60 /**1**	0.12/**6**	0.92/**3**	1.47/**2**	0.29/**6**	6.65/**1**	1.75/**6**

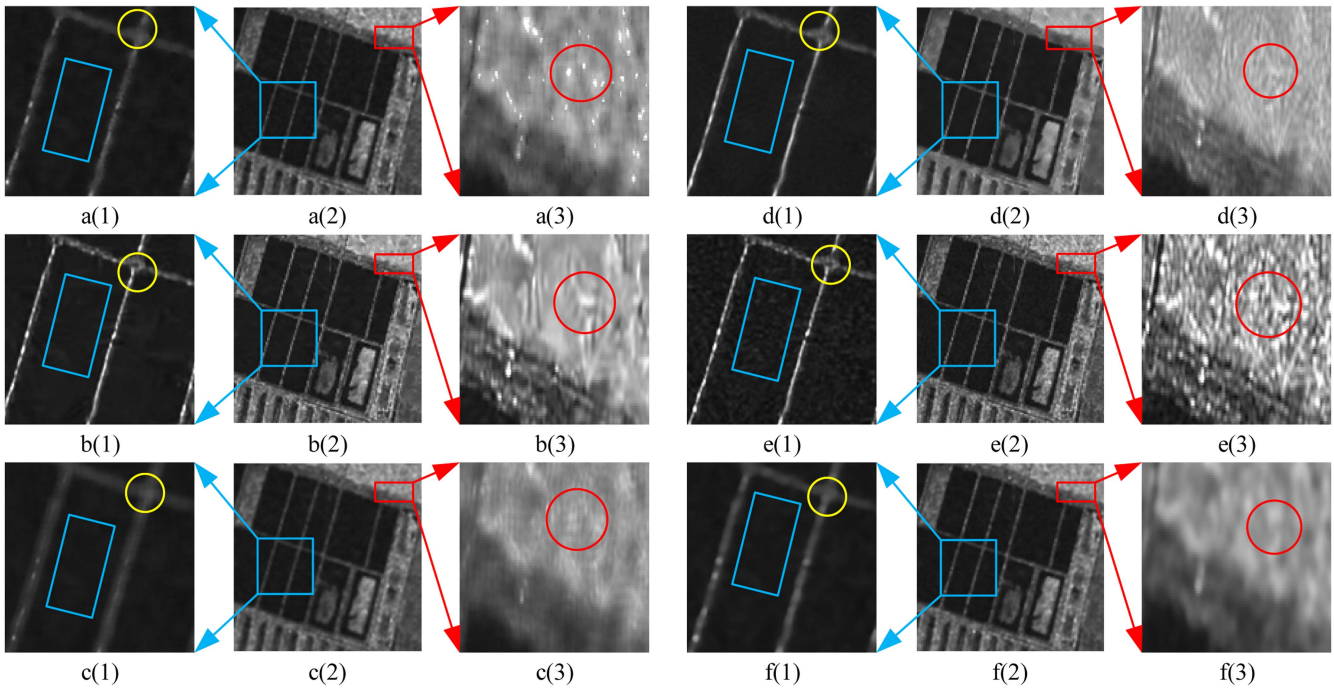

Fig. 9. Filtered TerraSAR-X SAR image by a(2) EnLee, b(2) FANS, c(2) NLM, d(2) PPB, e(2) SARBM3D, and f(2) SRAD. The first, third, fourth, and sixth columns are zoomed-in displays of the corresponding filters, respectively.

TABLE IV
ASSESSMENT METRICS AND RANKING FOR THE GF-3 IMAGE

Filters	ENL	SMPI	CENL	ESI	SSIM	HoEF	HeEF	M	IQE_HHSP
EnLee	78.43/**5**	5.38/**3**	0.53/**5**	0.35/**1**	0.54/**4**	1.67/**5**	0.85/**3**	117.12/**6**	0.48/**4**
FANS	261.84/**1**	9.01/**5**	0.41/**1**	0.27/**3**	0.55/**2**	2.16/**1**	0.86/**2**	42.15/**5**	0.53/**1**
NLM	139.27/**3**	2.58/**2**	0.47/**3**	0.10/**5**	0.38/**6**	1.95/**3**	0.72/**5**	11.76/**1**	0.48/**3**
PPB	164.88/**2**	9.36/**6**	0.45/**2**	0.21/**4**	0.55/**3**	1.99/**2**	0.80/**4**	24.78/**2**	0.50/**2**
SARBM3D	36.41/**6**	7.09/**4**	0.64/**6**	0.33/**2**	0.75/**1**	.1.04/**6**	0.88/**1**	40.28/**4**	0.40/**6**
SRAD	112.65/**4**	0.71 /**1**	0.49 /**4**	0.08/**6**	0.43/**5**	1.70/4	0.72/**6**	24.99/**3**	0.45/**5**

phenomenon compared with EnLee. This demonstrates a higher degree of matching between HoEF and HVS. HeEF, proposed along with the traditional SSIM index, indicated that SARBM3D and FANS have better edge preservation than the other methods, with SARBM3D showing more abundant texture than FANS. EnLee exhibits significant local nonuniformity and higher contrast compared with PPB. Therefore, EnLee scored higher on the HeEF index than PPB. There was a discrepancy between HeEF and SSIM in evaluating edge preservation between NLM and SRAD. SRAD showed more severe edge loss than NLM, making HeEF more visually convincing, which can be clearly seen from the red rectangles in c(3) and f(3) of Fig. 7. The ESI and SMPI indicators were not well validated in this experiment. This analysis validates the effectiveness of HoEF and HeEF in evaluating speckle suppression and edge information preservation. Better speckle smoothing often leads to greater edge loss, underscoring the importance of considering both aspects in evaluating filtering models.

The proposed IQE_HHSP indicator indicated that SARBM3D had the poorest overall performance due to its noticeable undersmoothing phenomenon. SRADs slightly lower score in IQE_HHSP compared with NLM was due to its noticeable pseudotexture phenomenon and more edge loss. FANS performed better than EnLee and PPB in HoEF and

TABLE V
ASSESSMENT METRICS AND RANKING FOR THE TERRASAR-X IMAGE

Filters	ENL	SMPI	CENL	ESI	SSIM	HoEF	HeEF	M	IQE_HHSP
EnLee	29.88/**5**	1.32/**2**	0.68/**5**	0.13/**4**	0.47/**4**	1.51/**3**	0.46/**4**	6.13/**1**	5.63/**3**
FANS	31.59/**4**	7.86/**6**	0.67/**4**	0.27/**2**	0.71/**2**	1.51/**4**	0.56/**2**	8.00/**3**	5.77/**1**
NLM	43.07/**2**	1.70/**3**	0.61/**2**	0.08/**5**	0.38/**6**	1.64/**2**	0.41/**6**	7.44/**2**	5.59/**4**
PPB	49.11/**1**	7.71/**5**	0.59/**1**	0.18/**3**	0.61/**3**	1.71/**1**	0.47/**3**	12.47/**5**	5.73/**2**
SARBM3D	8.48/**6**	6.08/**4**	1.08/**6**	0.38/**1**	0.87/**1**	0.57/**6**	0.59/**1**	24.60/**6**	5.45/**6**
SRAD	34.61/**3**	0.77/**1**	0.65/**3**	0.08/**6**	0.46/**5**	1.41/**5**	0.42/**5**	9.01/**4**	5.53/**5**

HeEF, indicating significantly better overall performance. PPB excelled in speckle smoothing compared with EnLee, placing PPB ahead in comprehensive indicators. While the *M* indicator suggested that NLM achieved the best overall evaluation effect, this was not substantiated by visual assessment or other indicator evaluations.

In summary, the IQE_HHSP metrics aligned with the actual situation in evaluating individual and overall metrics, confirming the effectiveness of the IQE_HHSP metrics in evaluating the GF-3 filtered image.

D. Evaluation Experiments of TerraSAR-X Image Filtering Models

The filtered images and local zoomed-in areas of the TerraSAR-X images are displayed in Fig. 9. The corresponding metrics evaluation results and rankings are shown in Table V, where the metric evaluation rankings are marked in bold.

Visually, all six filtering models effectively suppressed speckle. From the enlarged areas in the third and sixth columns, as shown in Fig. 9, it is evident that PPB and NLM exhibited the most effective speckle-smoothing effects. Among these, PPB demonstrated superior smoothness compared with NLM. EnLee and FANS showed similar smoothing effects, while SRAD exhibited significant oversmoothing. The pseudotexture of SARBM3D remained pronounced. Considering edge-preserving information, SARBM3D retained the most edge information, followed by FANS. PPB experienced some loss of edge information, and EnLee exhibited significant local uneven strength values. The loss of edge information was most severe with NLM and SRAD.

From a quantitative evaluation perspective, HoEF, ENL, and CENL maintained a high degree of consistency; however, there were discrepancies in speckle suppression evaluation between EnLee and SRAD. The oversmoothing phenomenon of SRAD was more pronounced than that of EnLee (see Fig. 9). The evaluation results of the other filtering models were consistent with the observed outcomes. In terms of HeEF, ESI, and SSIM indices, SARBM3D achieved the best edge-preservation effect, while FANS yielded suboptimal results. Due to the local nonuniformity in EnLee's results, its contrast is better than PPB, and PPB has less edge loss than EnLee, and PPB and EnLee have comparable effects. The edge loss of NLM and SRAD was not clearly distinguished between ESI and HeEF, consistent with conclusions drawn from the HVS.

Overall, the proposed HoEF and HeEF metrics are roughly consistent with traditional measures, affirming their rationality and feasibility for speckle suppression and edge information evaluation in TerraSAR-X images.

Considering speckle suppression and edge-preservation metrics, both *M* and the proposed IQE_HHSP indicators indicated that SARBM3D had the poorest filtering performance. While FANS and PPB exhibited the overall effective outcomes, PPB demonstrated more severe pseudotexture and edge loss phenomena compared with FANS. Consequently, FANS outperformed PPB in the IQE_HHSP indicator. The HeEF metrics of NLM and SRAD yielded lower scores, rendering these methods less advantageous for the IQE_HHSP index. The speckle-smoothing effect of SRAD was inferior to that of NLM, resulting in superior comprehensive effect of NLM compared with SRAD. EnLee's HoEF index exceeded FANS, while HeEF index was comparable with PPB, but did not show outstanding performance in either index. However, the overall effect of EnLee was still better than the other three methods.

In summary, the performance of the IQE_HHSP metrics was consistent with the HVS and akin to previous evaluation metrics, validating the rationality and effectiveness of the IQE_HHSP metrics in assessing the filtering model of TerraSAR-X images.

E. Evaluation Experiments of Sentinel-1 Image Filtering Models

The filtering result map of the Sentinel-1 image and the local zoomed area are displayed in Fig. 10. The corresponding metric evaluation results and rankings are listed in Table VI, with the metric evaluation rankings marked in bold.

Visually, all six selected filtering models effectively achieved speckle suppression. From the perspective of speckle smoothing, PPB and NLM achieved the best and suboptimal results, respectively. Both EnLee and SRAD exhibited significant oversmoothing, with SRADs oversmoothing being more pronounced in the filtered image. Both FANS and SARBM3D exhibit nonuniformity and pseudotexture phenomena in the filtered images, with SARBM3D exhibiting a more pronounced undersmoothing phenomenon. For edge preservation, SARBM3D and FANS maintained less edge loss, with FANS exhibiting a more pronounced edge loss. EnLee still exhibited uneven strength values, and the filtering results of PPB showed an evident pseudotexture phenomenon. NLM and SRAD exhibited significant edge loss. From a quantitative perspective, the HoEF, ENL, and CENL indicators were partly the same; however, there were differences in the speckle-smoothing results for EnLee and SRAD. The evaluation results of the HeEF indicator were the same as those of the traditional ESI and SSIM indicators. From the perspective of speckle smoothing, the oversmoothing phenomenon of

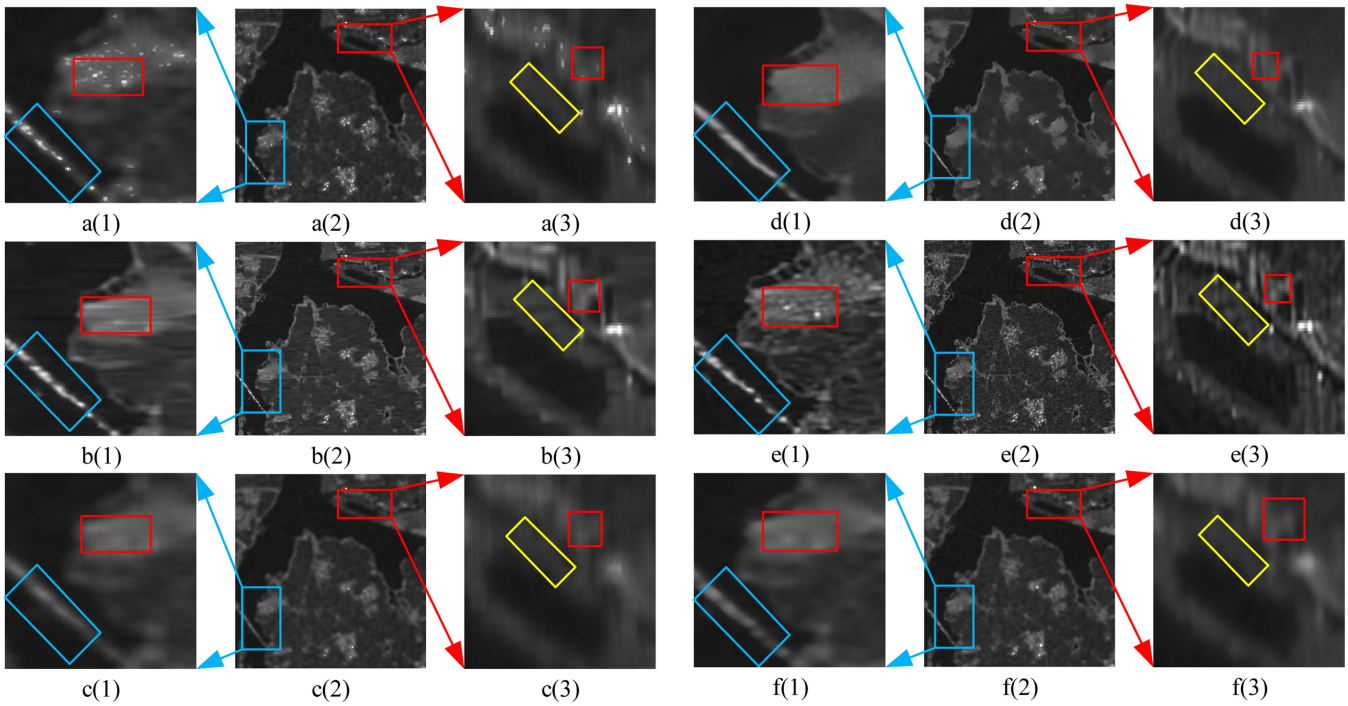

Fig. 10. Filtered Sentinel-1 SAR image by a(2) EnLee, b(2) FANS, c(2) NLM, d(2) PPB, e(2) SARBM3D, and f(2) SRAD. The first, third, fourth, and sixth columns are zoomed-in displays of the corresponding filters, respectively.

TABLE VI
ASSESSMENT METRICS AND RANKING FOR SENTINEL-1 IMAGE

Filters	ENL	SMPI	CENL	ESI	SSIM	HoEF	HeEF	M	IQE_HHSP
EnLee	110.60/**4**	0.98/**3**	0.49/**4**	0.24/**3**	0.65/**3**	1.03/**3**	0.63/**3**	70.64/**2**	3.97/**2**
FANS	94.50/**5**	5.85/**6**	0.51/**5**	0.28/**2**	0.76/**2**	0.72/**5**	0.66/**2**	112.27/**5**	3.87/**3**
NLM	162.40/**2**	0.44/**2**	0.45/**2**	0.13/**6**	0.56/**6**	1.04/**2**	0.57/**6**	62.56/**1**	3.87/**4**
PPB	465.65/**1**	1.57/**5**	0.37/**1**	0.15/**4**	0.65/**4**	1.34/**1**	0.62/**4**	94.19/**4**	4.06/**1**
SARBM3D	33.72/**6**	1.31/**4**	0.65/**6**	0.44/**1**	0.91/**1**	0.37/**6**	0.70/**1**	214.72/**6**	3.80/**6**
SRAD	136.47/**3**	0.29/**1**	0.47/**3**	0.14/**5**	0.64/**5**	0.98/**4**	0.59/**5**	78.50/**3**	3.86/**5**

TABLE VII
ASSESSMENT METRICS AND RANKING FOR RADARSAT-2 IMAGE

Filters	ENL	SMPI	CENL	ESI	SSIM	HoEF	HeEF	M	IQE_HHSP
EnLee	119.60/**5**	1.37/**2**	0.48/**5**	0.09/**5**	0.20/**6**	1.86/**4**	0.56/**4**	7.80/**3**	1.28/**5**
FANS	436.77/**1**	33.41/**5**	0.38/**1**	0.14/**3**	0.29/**2**	2.30/**1**	0.62/**3**	14.04/**5**	1.40/**2**
NLM	144.30/**4**	10.20/**3**	0.46/**3**	0.33/**1**	0.44/**3**	2.14/**3**	0.69/**1**	95.89/**6**	1.44/**1**
PPB	280.36/**2**	34.86/**6**	0.41/**2**	0.11/**4**	0.29/**4**	2.27/**2**	0.54/**5**	7.54/**2**	1.32/**3**
SARBM3D	77.10/**6**	29.92/**4**	0.53/**6**	0.24/**2**	0.57/**1**	1.40/**6**	0.65/**2**	12.01/**4**	1.30/**4**
SRAD	156.04/**3**	0.72/**1**	0.46/**4**	0.05/**6**	0.21/**5**	1.78/**5**	0.51/**6**	7.36/**1**	1.22/**6**

SRAD was more severe, resulting in lower HoEF indicator scores. From the perspective of edge preservation, EnLee's HeEF index is higher than PPB mainly due to EnLee's strong contrast. From the perspective of comprehensive indicators, the scores of the six filtering models in IQE_HHSP were consistent with their total rankings in the subindicators. However, the lowest ranking achieved by SARBM3D depended on its evident undersmoothing phenomenon, which was consistent with the evaluation results of the *M* indicator. In summary, the proposed IQE_HHSP was an effective Sentinel-1 image filter evaluation method.

F. Evaluation Experiments of Radarsat-2 Image Filtering Models

The filtering result maps of the Radarsat-2 images and local zoomed-in areas were displayed in Fig. 11 and the corresponding metric evaluation results and rankings were listed in Table VII, where the metric evaluation rankings were marked in bold.

From a visual perspective, the overall filtering situation, as shown in Fig. 11, indicates that all six filtering models can effectively achieve speckle suppression. From the enlarged areas displayed in the first and fourth columns, FANS and PPB showed

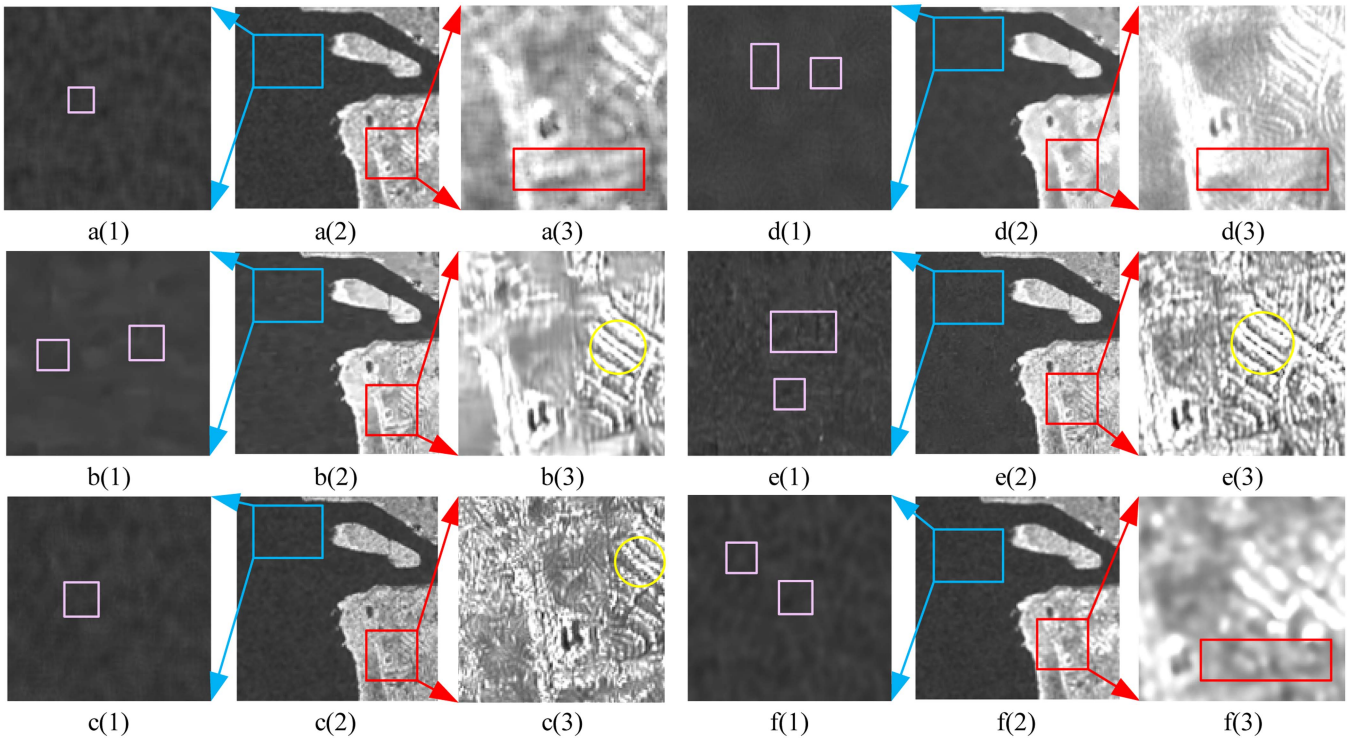

Fig. 11. Filtered Radarsat-2 SAR image by a(2)EnLee, b(2) FANS, c(2) NLM, d(2) PPB, e(2) SARBM3D, and f(2) SRAD. The first, third, fourth, and sixth columns are zoomed-in displays of the corresponding filters, respectively.

good smoothing performances, with PPB showing a slight pseudotexture phenomenon. EnLee, NLM, SARBM3D, and SRAD exhibited varying degrees of nonuniformity, with NLM being the least severe and SARBM3D the most severe. From a(3) and f(3) of Fig. 11, it can be seen that the oversmoothing phenomenon in the image after SRAD filtering was more severe than that in EnLee. In terms of edge loss, NLM retained the most information, followed by SARBM3D and FANS. EnLee and PPB resulted in significant amount of information loss, with SRAD experiencing the highest degree of information loss. From a quantitative perspective, HoEF, traditional ENL, and CENL believe that FANS and PPB achieved the best and suboptimal smoothing effects, whereas SARBM3D exhibited the poorest smoothing effect. The unevenness of NLM was lower than the above two methods, and the smoothness is better than EnLee and SRAD, while the oversmoothing phenomenon of SRAD is more severe than EnLee. Therefore, NLM, EnLee, and SRAD ranked third, fourth, and fifth, respectively, on the HoEF index. From the perspective of edge-preservation indicators, both HeEF and ESI believed that NLM, SARBM3D, and FANS achieved the top three results, which were verified by the visual interpretation mentioned above. The information lost by the SRAD can be validated in the filtered images. The main reason why EnLee ranks higher than PPB in the HeEF index is that the contrast of EnLee results is significantly higher than that of PPB. Finally, we comprehensively considered both speckle smoothing and edge preservation. The scores of each indicator in the IQE_HHSP were approximately the same as their total rankings in the subindicators. Because speckle smoothness of NLM is comparable with that of the FANS and its relatively richer edge information, the NLM scores are higher than those of the FANS in IQE_HHSP.

Overall, there was a high degree of consistency between the IQE_HHSP indicator and the HVS, which verifies the effectiveness of the IQE_HHSP indicator in evaluating Radarsat-2 filtered images.

V. Discussion

A. Experiment on Effect of Homogeneous Patch Extraction on HoEF

In the four real SAR image experiments, the MRSGCM strategy effectively extracts the homogeneous and heterogeneous patches, which provides the accurate experimental basis for the partition evaluation, and the partition evaluation results match well with the actual situation and popularity indices, thus verifying the validity and reasonableness of the proposed method in this article.

The selection of homogeneous and heterogeneous patches is crucial for homogeneous and heterogeneous patch evaluation. Within the framework of the MRSGCM experiment, the default parameters were established as follows: $T1 = 0.95$, $T2 = 0.8$, $H1 = 0.9$, and $H2 = 0.1$. Given that the evaluation experiment for SAR filtering models does not necessitate the extraction of all patches, the determination of the aforementioned threshold exhibits considerable subjectivity. In this section, we will explore the influence that the quantity of homogeneous patch has on the evaluation outcomes and selects a more intuitive model

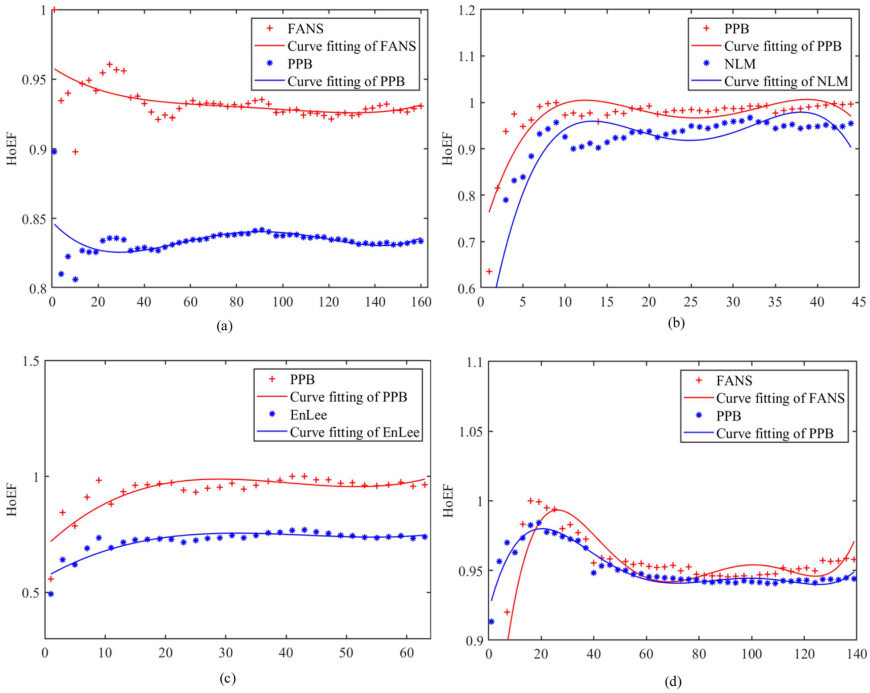

Fig. 12. Relationship between the number of homogeneous patches and HoEF indicator. (a) Number of homogeneous patches obtained in GF-3 image. (b) Number of homogeneous patches obtained in TerraSAR-X image. (c) Number of homogeneous patches obtained in Sentinel-1 image. (d) Number of homogeneous patches obtained in Radarsat-2 image.

in the HoEF evaluation as a reference. The experimental results are presented in Fig. 12.

From Fig. 12(a), it can be seen that the speckle suppression effect of the FANS is better than that of the PPB. It can be observed that, as the number of homogeneous patches increases, the HoEF metrics of the FANS and PPB also stabilize, but the overall effect of the FANS is still better than that of the PPB. A similar conclusion can be obtained from Fig. 12(b); when there are more homogeneous patches, the filtering metrics tend to be more stabilized, and the effect of the PPB is not significantly different from that of the NLM; however, when the number of homogeneous zones is small, the metrics of the PPB are significantly better than those of the NLM. From Fig. 12(c), it can be seen that the overall indicators of the PPB are above EnLee and do not change with an increase in the number of homogeneous patches, but the magnitude of the difference decreases. As shown in Fig. 12(d), when the number of homogeneous patches was less than 25, the PPB effect was significantly better than that of the FANS; however, when the number of homogeneous patches was greater than 25, the effect of the FANS and PPB was inverted, and there was no significant change in the difference between the FANS and PPB as the number continued to increase.

To verify the conclusions obtained above, ENL metrics were selected for comparison, and the relationship between the ENL metrics and the number of homogeneous patches is plotted in Fig. 13. It can be observed from Fig. 13(b)–(d) that with an increase in the number of homogeneous patches, the gap between the two filtering models decreases, and the performance of the ENL gap of the two filtering models with a change in the number of homogeneous patches in Fig. 13(a) is not obvious. As can be seen from the result plots of the Sentinel-1 image, when the number of homogeneous patches is selected to be approximately 25, the difference between the ENL metrics of the two filtering models reaches a maximum, which is slightly different from that of the HoEF metrics, indicating that the ENL metrics are severely affected by the smoothing image, and that a high ENL does not represent a high speckle suppression. From the above results, it can be observed that the number of homogeneous patches has an impact on the evaluation of homogeneous patches. From the above results, it can be observed that the number of homogeneous regions has a certain degree of impact on the evaluation of HoEF indicators. However, when a certain number of homogeneous regions are selected (such as 25), the impact of the number of regions on the evaluation will be negligible. Obtaining an HoEF that matches the visual effect by accurately selecting the number of homogeneous patches is crucial. The threshold recommended in this article can minimize this impact to the greatest extent possible, but this is still the focus of future research.

The HeEF metrics were carried out for heterogeneous patches, and the results were similar to those of the ESI and SSIM metrics because the above three metrics were constructed by utilizing the brightness, contrast, structure, and texture information of the images before and after filtering to construct a similar function model and obtain the final results through the model constraints. Therefore, these three methods are consistent with the visual effect; however, there is a subtle gap between some of the filtering models, which is well portrayed by the method in this study. In the overall assessment, the proposed IQE_HHSP index combines more with the visual effect; therefore, it is more in line

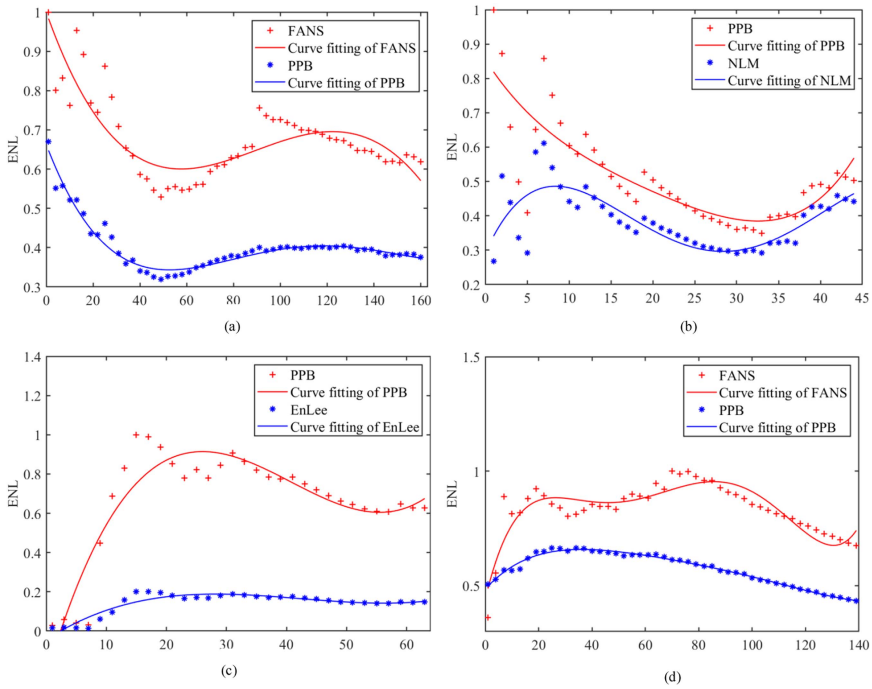

Fig. 13. Relationship between the number of homogeneous patches and ENL indicator. (a) Number of homogeneous patches obtained in GF-3 image. (b) Number of homogeneous patches obtained in TerraSAR-X image. (c) Number of homogeneous patches obtained in Sentinel-1 image. (d) Number of homogeneous patches obtained in Radarsat-2 image.

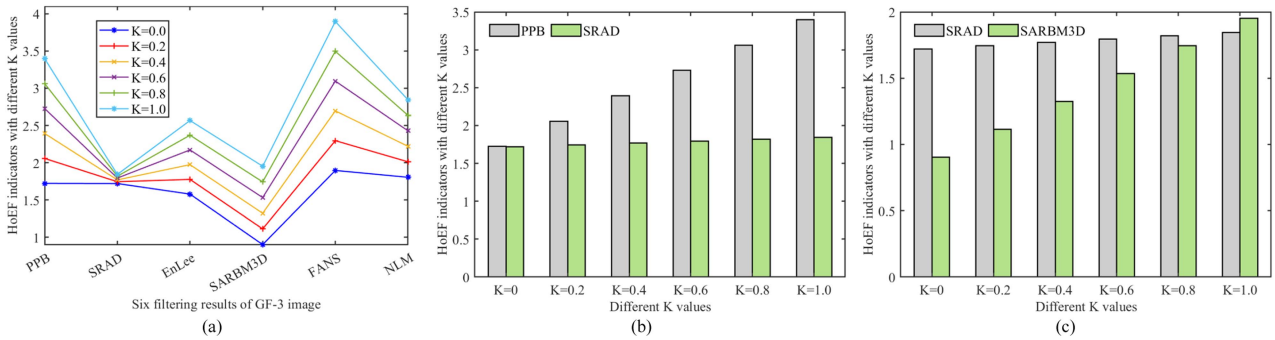

Fig. 14. (a) HoEF index of different K values in GF-3 image. (b) The HoEF values of PPB and SRAD methods for different K values. (c) The HoEF values of SRAD and SARBM3D methods for different K values.

with the actual situation than the M index. However, the overall model is still affected by the number of homogeneous patches extracted and needs to be weighted according to the number of homogeneous patches. Therefore, subsequent experiments are required to further investigate the optimal number of homogeneous and heterogeneous patches.

B. *Sensitivity Experiment of* K *Value to HoEF Index*

In the homogeneous patch evaluation experiment, K represents the weight of the fuzzy index. However, further analysis is needed to determine the optimal range for K values. Therefore, this section conducts corresponding experimental analysis on the influence of K value on HoEF index and selects six filtering results of GF-3 image as the presentation, as shown in Fig. 14(a). To verify the effectiveness of K, comparative experiments were conducted using PPB and SRAD, as well as SRAD and SARBM3D. The results are presented in Fig. 14(b) and (c).

From Fig. 14(a), it can be seen that as the K value changes, there is no significant change in the relative relationship between the HoEF indicators obtained by the six filtering methods, but there is a significant change in the relative differences between the various methods. From Fig. 14(b), it can be seen that, as the K value increases, the difference between the HoEF indicators obtained by PPB and SRAD methods also increases. When $K = 0$, the HoEF indicators of both are comparable, which is clearly inconsistent with the conclusion, as obtained in Fig. 8, thus verifying the importance of the K value. From Fig. 14(c), it can be seen that the difference in HoEF values

TABLE VIII
TIME COMPLEXITY OF EVALUATION INDICATORS FOR GF-3 IMAGE

Filters	ENL	SMPI	CENL	ESI	SSIM	HoEF	HeEF	M	IQE_HHSP
EnLee	0.001	0.002	0.01	0.021	0.011	0.439	0.079	0.422	0.594
FANS	0.001	0.001	0.009	0.014	0.006	0.428	0.090	0.430	0.589
NLM	0.002	0.001	0.009	0.014	0.006	0.424	0.076	0.431	0.616
PPB	0.002	0.003	0.014	0.038	0.018	0.565	0.150	0.540	0.764
SARBM3D	0.002	0.001	0.011	0.014	0.006	0.438	0.079	0.432	0.616
SRAD	0.001	0.002	0.009	0.013	0.005	0.447	0.084	0.429	0.624

obtained by SRAD and SARBM3D filtering becomes smaller as the K value increases. When $K = 1.0$, the HoEF value obtained by SARBM3D exceeds that of the SRAD method. However, it can be clearly seen from Fig. 8 that the filtering method of SRAD is superior to SARBM3D, which also proves that a high K value can cause misjudgment. In order to align the evaluation results more with visual assessment, the recommended range for K value is [0.1, 0.5]. The comparative experiment selects the one with more obvious effects as the display, and other experiments can also obtain the same conclusion as the above analysis.

C. Time Complexity Experiment for Proposed Method

Section IV conducted corresponding algorithm validation experiments on the proposed method, verifying its effectiveness in speckle suppression and edge preservation. This section will evaluate the time complexity of the algorithm. GF-3 images were selected as the test data for the experiment. The experimental results are shown in Table VIII. From Table VIII, it can be seen that ENL and SSIM perform relatively well in terms of algorithm time consumption, followed by SMPI, CENL, and ESI. HoEF and HeEF have relatively high time consumption. From the perspective of overall indicator complexity, IQE_HHSP takes more time than the M index. This is due to the use of multiangle evaluation in the IQE_HHSP method, which increases the complexity of the algorithm. Although the IQE_HHSP method takes relatively more time compared with other classical evaluation metrics, its good evaluation performance certainly holds advantages. In addition, subsequent experiments will also reduce complexity through program optimization and parallel computing.

VI. CONCLUSION

The accurate evaluation of SAR image filtering performance is an important prerequisite for high-quality SAR applications. To better evaluate whether a filter can meet the requirements of keeping the target constant in homogeneous patches and retaining detailed information in heterogeneous patches, this study proposed a homogeneous and heterogeneous field-adaptive extraction SAR filter quality evaluation index (IQE_HHSP). In this study, the homogeneous and heterogeneous patches were well distinguished using the MRSGCM strategy, and the partition evaluation was realized in two parts: HoEF and HeEF. The effectiveness of IQE_HHSP was verified using four real SAR images with six quality assessment indices. However, when evaluating the overall performance indicators, it is crucial to also consider the significance of individual performance indicators, such as HoEF and HeEF. A thorough analysis should not be solely dependent on composite indicators, as this could potentially obscure the distinctive contributions and inherent limitations of each individual metric. By examining individual indicators, the intricacies of filtering model performance can be more comprehensively and meticulously analyzed. The experimental findings further demonstrate that both the individual and comprehensive indicators have validated the efficacy of the method presented in this article in evaluating the quality of SAR image filtering models.

ACKNOWLEDGMENT

The authors would like to thank the anonymous reviewers for their valuable comments and insightful suggestions, which greatly contributed to the improvement of this study.

REFERENCES

[1] X. Ma, H. Shen, X. Zhao, and L. Zhang, "SAR image despeckling by the use of variational methods with adaptive nonlocal functionals," *IEEE J. Sel. Topics Appl. Earth Observ. Remote Sens.*, vol. 54, no. 6, pp. 3421–3435, Jun. 2016.

[2] F. Lang, J. Yang, D. Li, L. Shi, and J. Wei, "Mean-shift-based speckle filtering of polarimetric SAR data," *IEEE Trans. Geosci. Remote Sens.*, vol. 52, no. 7, pp. 4440–4454, Jul. 2014.

[3] G. Di Martino, M. Poderico, G. Poggi, D. Riccio, and L. Verdoliva, "Benchmarking framework for SAR despeckling," *IEEE Trans. Geosci. Remote Sens.*, vol. 52, no. 3, pp. 1596–1615, Mar. 2014.

[4] F. Guo, C. Sun, N. Sun, X. Ma, and W. Liu, "Integrated quantitative evaluation method of SAR filters," *Remote Sens.*, vol. 15, no. 5, Mar. 2023, Art. no. 1409.

[5] L. Bu, S. Zhao, and Z. Zhang, "Multi-temporal SAR image denoising method with NLM and ratio image," *Remote Sens. Inf.*, vol. 36, no. 3, pp. 17–24, 2021.

[6] Z. Sun, Z. Zhang, Y. Chen, S. Liu, and Y. Song, "Frost filtering algorithm of SAR images with adaptive windowing and adaptive tuning factor," *IEEE Geosci. Remote Sens. Lett.*, vol. 17, no. 6, pp. 1097–1101, Jun. 2020.

[7] J.-S. Lee, "Digital image enhancement and noise filtering by use of local statistics," *IEEE Trans. Pattern Anal. Mach. Intell.*, vol. PAMI-2, no. 2, pp. 165–168, Mar. 1980.

[8] J.-S. Lee, J.-H. Wen, T. L. Ainsworth, K.-S. Chen, and A. J. Chen, "Improved sigma filter for speckle filtering of SAR imagery," *IEEE Trans. Geosci. Remote Sens.*, vol. 47, no. 1, pp. 202–213, Jan. 2009.

[9] M. Yahia, T. Ali, M. M. Mortula, R. Abdelfattah, S. E. Mahdy, and N. S. Arampola, "Enhancement of SAR speckle denoising using the improved iterative filter," *IEEE J. Sel. Topics Appl. Earth Observ. Remote Sens.*, vol. 13, pp. 859–871, Feb. 2020.

[10] L. C. Neves, F. M. Ribas, J. M. Maia, A. J. Zimbico, A. A. Assef, and E. T. Costa, "Enhanced Wiener and Kuan filters applied with adaptive beamformers for improved contrast and resolution in ultrafast ultrasound images," in *Proc. IEEE Int. Ultrasonics Symp.*, Venice, Italy, 2022, pp. 1–4.

[11] R. Farhadiani, S. Homayouni, A. Bhattacharya, and M. Mahdianpari, "SAR despeckling based on CNN and Bayesian estimator in complex wavelet domain," *IEEE Geosci. Remote Sens. Lett.*, vol. 19, Jun. 2022, Art. no. 4510005.

[12] G. Nandhini and C. Saraswathy, "Speckle suppression of SAR image based on curvelet and dual tree complex wavelet transform," in *Proc. Int. Conf. Inf. Commun. Embedded Syst.*, Chennai, India, 2013, pp. 650–654.

[13] S. Liu et al., "SAR speckle removal using hybrid frequency modulations," *IEEE Trans. Geosci. Remote Sens.*, vol. 59, no. 5, pp. 3956–3966, May 2021.
[14] S. Liu, M. Liu, P. Li, J. Zhao, Z. Zhu, and X. Wang, "SAR image denoising via sparse representation in shearlet domain based on continuous cycle spinning," *IEEE Trans. Geosci. Remote Sens.*, vol. 55, no. 5, pp. 2985–2992, May 2017.
[15] S. Baraha and A. K. Sahoo, "Synthetic aperture radar image and its despeckling using variational methods: A review of recent trends," *Signal Process.*, vol. 212, Nov. 2023, Art. no. 659852.
[16] F. Guo, C. Zhou, W. Liu, and Z. Liu, "Pixel difference function and local entropy-based speckle reducing anisotropic diffusion," *IEEE Trans. Geosci. Remote Sens.*, vol. 60, Jun. 2022, Art. no. 5229516.
[17] Y. J. Yu and S. T. Acton, "Speckle reducing anisotropic diffusion," *IEEE Trans. Image Process.*, vol. 11, no. 11, pp. 1260–1270, Nov. 2002.
[18] K. Mei, B. Hu, B. Fei, and B. Qin, "Phase asymmetry ultrasound despeckling with fractional anisotropic diffusion and total variation," *IEEE Trans. Image Process.*, vol. 29, pp. 2845–2859, 2020.
[19] F. Guo et al., "Fusion despeckling based on surface variation anisotropic diffusion filter and ratio image filter," *IEEE Trans. Geosci. Remote Sens.*, vol. 58, no. 4, pp. 2398–2411, Apr. 2020.
[20] G. Zhang, F. Guo, Q. Zhang, K. Xu, P. Jia, and X. Hao, "Speckle reduction by directional coherent anisotropic diffusion," *Remote Sens.*, vol. 11, no. 23, Nov. 2019, Art. no. 2768.
[21] J. Zhang et al., "Coherent speckle anisotropic diffusion suppression by fusing multi-directional Sobel operators," *Remote Sens. Technol. Appl.*, vol. 38, no. 5, pp. 1118–1125, Nov. 2023.
[22] A. Buades., B. Coll., and J. M. Morel, "A non-local algorithm for image denoising," in *Proc. IEEE Comput. Soc. Conf. Comput. Vis. Pattern Recognit.*, San Diego, CA, USA, 2005, pp. 60–65.
[23] F. Guo, H. Tang, and W. Liu, "Non-local means de-speckling based on multi-directional local plane inclination angle," *Remote Sens.*, vol. 15, no. 4, Feb. 2023, Art. no. 1029.
[24] S. Parrilli, M. Poderico, C. V. Angelino, and L. Verdoliva, "A nonlocal SAR image denoising algorithm based on LLMMSE wavelet shrinkage," *IEEE Trans. Geosci. Remote Sens.*, vol. 50, no. 2, pp. 606–616, Feb. 2012.
[25] D. Cozzolino, S. Parrilli, G. Scarpa, G. Poggi, and L. Verdoliva, "Fast adaptive nonlocal SAR despeckling," *IEEE Geosci. Remote Sens. Lett.*, vol. 11, no. 2, pp. 524–528, Feb. 2014.
[26] C.-A. Deledalle, L. Denis, and F. Tupin, "Iterative weighted maximum likelihood denoising with probabilistic patch-based weights," *IEEE Trans. Image Process.*, vol. 18, no. 12, pp. 2661–2672, Dec. 2009, doi: 10.1109/TIP.2009.2029593.
[27] G. Baier, W. He, and N. Yokoya, "Robust nonlocal low-rank SAR time series despeckling considering speckle correlation by total variation regularization," *IEEE Trans. Geosci. Remote Sens.*, vol. 58, no. 11, pp. 7942–7954, Nov. 2020.
[28] S. Liu, Y. Lei, L. Zhang, B. Li, W. Hu, and Y.-D. Zhang, "MRDDANet: A multiscale residual dense dual attention network for SAR image denoising," *IEEE Trans. Geosci. Remote Sens.*, vol. 60, 2022, Art. no. 5214213.
[29] H. Lin, Y. Zhuang, Y. Huang, and X. Ding, "Self-supervised SAR despeckling powered by implicit deep denoiser prior," *IEEE Geosci. Remote Sens. Lett.*, vol. 19, Oct. 2022, Art. no. 4514705.
[30] E. Dalsasso, L. Denis, and F. Tupin, "As if by magic: Self-supervised training of deep despeckling networks with MERLIN," *IEEE Trans. Geosci. Remote Sens.*, vol. 60, 2022, Art. no. 4704713.
[31] A. G. Mullissa, D. Marcos, D. Tuia, M. Herold, and J. Reiche, "deSpeckNet: Generalizing deep learning-based SAR image despeckling," *IEEE Trans. Geosci. Remote Sens.*, vol. 60, 2022, Art. no. 5200315.
[32] X. Ma, C. Wang, Z. Yin, and P. Wu, "SAR image despeckling by noisy reference-based deep learning method," *IEEE Trans. Geosci. Remote Sens.*, vol. 58, no. 12, pp. 8807–8818, Dec. 2020.
[33] S. Vitale, G. Ferraioli, A. C. Frery, V. Pascazio, D.-X. Yue, and F. Xu, "SAR despeckling using multiobjective neural network trained with generic statistical samples," *IEEE Trans. Geosci. Remote Sens.*, vol. 61, Sep. 2023, Art. no. 5216812.
[34] C. Oliver and S. Quegan, *Understanding Synthetic Aperture Radar Images*. London, U.K.: SciTech Publishing, 2004.
[35] Y. Sheng and Z. Xia, "A comprehensive evaluation of filters for radar speckle suppression," in *Proc. IEEE Int. Geosci. Remote Sens. Symp.*, Lincoln, NE, USA, 1996, pp. 1559–1561.
[36] A. Shamsoddini and J. Trinder, "Image texture preservation in speckle noise suppression," *ISPRS J. Photogramm. Remote Sens.*, vol. 38, pp. 239–244, Jul. 2010.
[37] S. G. Dellepiane and E. Angiati, "Quality assessment of despeckled SAR images," *IEEE J. Sel. Topics Appl. Earth Observ. Remote Sens.*, vol. 7, no. 2, pp. 691–707, Feb. 2014.
[38] Z. Wang, A. C. Bovik, H. R. Sheikh, and E. P. Simoncelli, "Image quality assessment: From error visibility to structural similarity," *IEEE Trans. Image Process.*, vol. 13, no. 4, pp. 600–612, Apr. 2004.
[39] L. Tang, P. Jiang, and C. Dai, "A comparative study of the effectiveness of speckle noise removal methods for satellite-borne SAR images," *Remote Sens. Environ.*, vol. 11, no. 3, pp. 206–211, Aug. 1996.
[40] F. Sattar, L. Floreby, G. Salomonsson, and B. Lovstrom, "Image enhancement based on a nonlinear multiscale method," *IEEE Trans. Image Process.*, vol. 6, no. 6, pp. 888–895, Jun. 1997.
[41] M. Hagara and A. Hlavatovic, "Video segmentation based on Pratt's figure of merit," in *Proc. 19th Int. Conf. Radioelektronika*, Bratislava, Slovakia, 2009, pp. 91–94.
[42] X. Ma, H. Hu, and P. Wu, "A no-reference edge-preservation assessment index for SAR image filters under a Bayesian framework based on the ratio gradient," *Remote Sens.*, vol. 14, no. 4, Feb. 2022, Art. no. 856.
[43] L. Gomez, R. Ospina, and A. C. Frery, "Unassisted quantitative evaluation of despeckling filters," *Remote Sens.*, vol. 9, no. 4, Apr. 2017, Art. no. 389.
[44] L. Gomez, M. E. Buemi, J. C. Jacobo-Berlles, and M. E. Mejail, "A new image quality index for objectively evaluating despeckling filtering in SAR images," *IEEE J. Sel. Topics Appl. Earth Observ. Remote Sens.*, vol. 9, no. 3, pp. 1297–1307, Mar. 2016.
[45] A. Achim, E. E. Kuruoglu, and J. Zerubia, "SAR image filtering based on the heavy-tailed Rayleigh model," *IEEE Trans. Image Process.*, vol. 15, no. 9, pp. 2686–2693, Sep. 2006.
[46] J. Ni, *Research on SAR Image Filtering Algorithm and New Evaluation Model*. Xi'an, China: Xi'an Univ. of Electronic Science and Technology, 2018.
[47] J. Guan, W. Zhang, J. Gu, and H. Ren, "No-reference blur assessment based on edge modeling," *J. Vis. Commun. Image Representation*, vol. 29, May 2015, Art. no. 269854.
[48] X. Zou, Y. Zhang, S. Zhang, and J. Zhang, "FPGA implementation of edge detection for Sobel operator in eight directions," in *Proc. IEEE Asia Pacific Conf. Circuits Syst.*, Chengdu, China, 2018, pp. 520–523.
[49] N. D. Narvekar and L. J. Karam, "A no-reference image blur metric based on the cumulative probability of blur detection (CPBD)," *IEEE Trans. Image Process.*, vol. 20, no. 9, pp. 2678–2683, Sep. 2011.
[50] D. Varga, "Full-reference image quality assessment based on Grünwald–Letnikov derivative, image gradients, and visual saliency," *Electronics*, vol. 11, no. 4, Feb. 2022, Art. no. 559.
[51] M. Gao, H. Dang, L. Wei, H. Wang, and Y. Zhang, "Image quality evaluation combining global and local variations," *J. Automat.*, vol. 46, no. 12, pp. 2662–2671, Dec. 2020.
[52] L. Zhang, X. Mou, and D. Zhang, "FSIM: A feature similarity index for image quality assessment," *IEEE Trans. Image Process.*, vol. 20, no. 8, pp. 2378–2386, Aug. 2011.

Chuang Sun was born in 2000. He received the B.E. degree in remote sensing science and technology in 2023 from Jiangsu Normal University, Xuzhou, China, where he is currently working toward the M.S. degree in cartography and Geographical Information System.

He majors in synthetic aperture radar (SAR) image processing.

Fengcheng Guo was born in 1992. He received the Ph.D. degree in photogrammetry and remote sensing from the State Key Laboratory of Information Engineering in Surveying Mapping, and Remote Sensing (LIESMRS), Wuhan University, Wuhan, China, in 2020.

Since 2020, he has been with the School of Geography, Geomatics and Planning, Jiangsu Normal University, where he became an Associate Professor in 2022. He majors in synthetic aperture radar image processing.

Zhaoling Hu was born in 1973. She received the Ph.D. degree in geodesy and surveying engineering from the China University of Mining and Technology, Beijing, China, in 2001.

She has been working with Jiangsu Normal University since 2001. She was appointed as a Professor in 2010. Her research interests include remote sensing information extraction and application.

Lianpeng Zhang received the M.S. degree in geodesy and survey engineering from the Shandong University of Science and Technology, Taian, China, in 1989, and the Ph.D. degree in photogrammetry and remote sensing from the Shandong University of Science and Technology, Qingdao, China, in 2003.

He is currently a Professor with the School of Geography, Geomatics and Planning, Jiangsu Normal University, Xuzhou, China. His research interests include high-resolution image processing and computer vision in urban remote sensing applications.

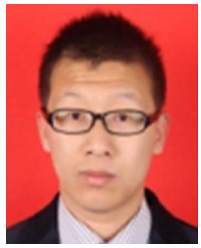

Wensong Liu received the M.S. degree in surveying and mapping from the China University of Petroleum, Qingdao, China, in 2016, and the Ph.D. degree in photogrammetry and remote sensing from Wuhan University, Wuhan, China, in 2019.

He is currently an Associate Professor and a Researcher with the School of Geography, Geomatics and Planning, Jiangsu Normal University, Xuzhou, China. His research interests include PolSAR images processing and change detection.

Tingting Huang was born in 2000. She received the B.E. degree in remote sensing science and technology in 2023 from Jiangsu Normal University, Xuzhou, China. she is currently working toward the M.E. degree in measurement science and technology from Guilin University of Technology, Guilin, China.

She majors in ocean color remote sensing.